Article:

He, P., Craig, T.J., Wen, Y. et al. (2026) A Multidecadal Catalog of Normal-Faulting Earthquakes Across the Tibetan Plateau Derived From InSAR and Body-Waveform Modeling: Insights Into the Plateau's Extensional Tectonics and Dynamics. Journal of Geophysical Research: Solid Earth, 131 (6). e2025JB031925. ISSN: 2169-9313

https://doi.org/10.1029/2025jb031925

A multidecadal catalog of normal-faulting earthquakes across the Tibetan Plateau derived from InSAR and body-waveform modeling: Insights into the plateau's extensional tectonics and dynamics

Ping He[1,2], Timothy J. Craig[2], Yangmao Wen[3], Tim J. Wright[2], John R. Elliott[2], Jin Fang[2]

1 School of Geophysics and Geomatics, China University of Geosciences, Wuhan, China, 430074

2 COMET, School of Earth and Environment, University of Leeds, Leeds, UK, LS2 9JT

3 School of Geodesy and Geomatics, Wuhan University, Wuhan, Hubei, China, 430079

Correspondence to: P. He, phe@cug.edu.cn

Author addresses

Ping He
School of Geophysics and Geomatics, China University of Geosciences, Wuhan, 388 Lumo Road, Wuhan, Hubei 430074, China
School of Earth and Environment, University of Leeds, Leeds, LS2 9JT, UK
phe@cug.edu.cn and p.he@leeds.ac.uk
Timothy J. Craig, Tim J. Wright, John R. Elliott, Jin Fang
COMET, School of Earth and Environment, University of Leeds, Leeds, LS2 9JT, UK
T.J.Craig@leeds.ac.uk; T.J.Wright@leeds.ac.uk; J.Elliott@leeds.ac.uk; eejf@leeds.ac.uk
Yangmao Wen
School of Geodesy and Geomatics, Wuhan University, 129 Luoyu Road, Wuhan, Hubei 430079, China
ymwen@sgg.whu.edu.cn

Key Points:

- We refine source models of 40 Mw ≥ 5.0 normal-faulting events on the Tibetan Plateau by integrating InSAR and body-waveform inversions.
- The varying dip angles of normal-faulting events across the plateau present challenges for simple models of uniform crustal extension.
- Normal-faulting events account for 82% ± 7% of the geodetic dilation strain, with the remaining strain (equivalent to Mw 6.9 ± 0.1) likely aseismic or unruptured.

Abstract: Normal-faulting structures are believed to play a significant role in accommodating large-scale continental extension across the Tibetan Plateau. However, the fine-scale details of active tectonic structures in this region and their relationships with plateau deformation patterns remain poorly constrained. To better understand the extensional tectonics of the plateau, we compile a multidecadal catalog of normal-faulting earthquakes, including 40 Mw ≥ 5 events since 1976, using interferometric synthetic aperture radar (InSAR) analysis and global synthetic body-waveform modeling (gWFM). Most events occurred along N–S-trending fault planes at depths shallower than 10 ± 2 km and are characterized by a single, roughly circular asperity, with an average rupture width-to-length ratio of 0.8. Approximately 80% of events have dip angles within 35–65° (± 10°), although one potential low-angle (< 35°) event and several high-angle (> 65°) events are also identified. The spatial distribution of dip angles does not support the proposed extensional patterns, such as the west–east sequential collapse model (dip angles increase from west to east) or the central axially symmetric model (dip angles decrease from the middle at 87°E to the two sides). We find that most events occurred at elevations above 5000 m, corresponding to regions of positive dilation strain. Approximately 82% ± 7% of the regional geodetic dilation strain can be accounted for by the seismic moment release of normal-faulting events. Finally, normal-faulting events are confined to a region bounded by the southern margin of the Indian indenter and the Manyi–Kunlun fault. They are distributed mainly across the interior of the plateau, away from the eastern and western tectonic syntaxes.

Plain Language Summary: Large-scale continental extension and widespread rifting across the Tibetan Plateau are commonly interpreted as the plateau's response to the north–south convergence between the Indian and Eurasian plates. However, the mechanics and variability of the normal faults involved remain poorly resolved. In this study, we investigate the behavior of these rifts during earthquakes by combining satellite radar observations with global body-waveform modeling, allowing us to assemble a half-century catalog of normal-faulting events. Our analysis reveals that the rifts do not conform to a single style of deformation pattern; instead, they display a broad range of behaviors, with seismicity concentrated primarily at shallow depths. Moreover, normal-faulting earthquakes represent only one component of how the plateau accommodates extension. Together, these results highlight the complexity of extensional deformation in the

Tibetan Plateau, which likely reflects the interplay of multiple driving forces, including gravitational potential energy, far-field boundary stresses, and buoyant support within the lower crust. A more refined understanding of how these rifts connect with deeper crustal processes is therefore essential for constraining the tectonic evolution of the plateau.

1. Introduction

The Tibetan Plateau, the highest and largest plateau on Earth, was formed by the collision of the Indian and Eurasian plates 55–65 Ma and has since been shaped by their continued convergence (e.g., Molnar & Tapponnier, 1975; Kapp et al., 2008; Shin et al., 2022). The boundaries of the plateau are defined by three major faults: the Himalayan thrust fault to the south, the Longmenshan thrust fault to the southeast, and the Altyn–Tagh–Haiyuan left-lateral strike-slip fault to the north (Figure 1). Ongoing compression makes the plateau one of the most geologically active regions in the world, characterized by widespread active faulting, intense deformation, and high levels of seismicity. Consequently, the Tibetan Plateau is central to studies of continent–continent collision dynamics, and research there has led to a range of orogenic theories (e.g., Tapponnier & Molnar, 1976; England & Houseman, 1986; Peltzer & Tapponnier, 1988; England & Molnar, 1997; Yin & Harrison, 2000). To accommodate N–S compression, the plateau undergoes major thrust and strike-slip faulting along its margins and significant extensional deformation in its interior. To explain this extension, various kinematic and dynamic models have been proposed, including gravitational collapse driven by gradients of gravitational potential energy (Molnar & Tapponnier, 1978; Liu & Yang, 2003); convective removal of mantle lithosphere (England & Houseman, 1989; Houseman & Molnar, 1997); delamination of the lithospheric mantle (Bird, 1979); lower crustal channel flow (Royden et al., 1997); oblique convergence and block extrusion (Tapponnier et al., 2001); northward underthrusting of the Indian plate (Styron et al., 2015; Craig et al., 2012, 2020); slab rollback and tearing of the subducting Indian plate (Davies & von Blanckenburg, 1995; Liang et al., 2016; Li & Song, 2018); large-scale Pacific and Sunda slab rollback (Schellart et al., 2019); and reduction in the convergence rate of the Indian plate (Yin, 2000).

Present-day geodetic observations reveal ongoing convergence across the plateau interior at an average rate of 10–14 mm/yr in the N20°E direction, accompanied by an extension rate of approximately 23 mm/yr along an azimuth of 110° (perpendicular to the shortening direction) (e.g., Wang et al., 2001; Zhang et al., 2004; Wang & Shen, 2020). Extension outpaces convergence, leading to dilation and crustal thinning (Molnar et al., 1998; Liang et al., 2013). This extension is accommodated by both conjugate strike-slip faults and N–S normal rifts, with no active thrust faults in the plateau interior (Armijo et al., 1986; Taylor & Yin, 2009; Yin & Taylor, 2021). Strike-slip faulting is localized along the crustal block boundaries during the plateau formation, characterized by long length scales (> 200 km), high slip rates (> 10 mm/yr), and large earthquakes (Mw ≥ 7) (Tapponnier et al., 2001; Taylor & Yin, 2009). In contrast, normal faulting began at approximately 20 Ma, after the plateau reached a height of approximately 5000 m (Currie et al., 2005), and generally exhibits smaller length scales (< 100 km), slower slip rates (< 5 mm/yr), and small to moderate earthquakes (5 < Mw < 7) (Taylor & Yin, 2009). Normal faulting appears to play a role comparable to that of conjugate strike-slip faulting in the strain partitioning-based crustal extension of the plateau (Elliott et al., 2010). Moreover, normal faulting has long been regarded as an indicator of the plateau's uplift history (Garzione et al., 2003), crustal magma-flow channels (e.g., Taylor & Yin, 2009; Yang et al., 2009; Pang et al., 2022), and deep dynamic processes (e.g., Cogan et al., 1998; Yin, 2000; England et al., 2013; Taylor et al., 2021). However, in situ geodetic and seismic observations in the plateau region remain sparse due to the harsh environment and rugged topography, particularly for N–S-trending normal faulting (e.g., Jiang et al., 2021; Chen et al., 2024). Consequently, the mechanisms governing fault kinematics, slip distribution, and strain partitioning during plateau extension are still not well resolved.

Earthquake source models provide essential information on seismic events, including locations, depths, centroid-moment tensors, strike, dip, rake, and rupture behavior. These parameters offer insights into local tectonic structure and the kinematics of faulting and crustal deformation. Since 1976, global seismic events have been systematically identified and compiled into routinely generated catalogs based on waveform data, such as those provided by the U.S. Geological Survey (USGS), the Global Centroid Moment Tensor (GCMT), and the International Seismological Center (ISC). Although these earthquake catalogs are widely used, their depth estimates and focal mechanisms remain poorly constrained, largely due to their reliance on automatic waveform phase picking (Sloan et al., 2011). Reliable source mechanisms are typically determined using manual body-waveform modeling. For example, Wimpenny and Watson (2021) compiled a global waveform-modeled earthquake catalog (gWFM) using synthetic body-waveform modeling, which has been shown to provide well-constrained source parameters for moderate- or small-magnitude events (e.g., Blom et al., 2023). However, the latest gWFM catalog (v1.2) is limited to events in the Tibetan Plateau prior to 2011. On the other hand, interferometric synthetic aperture radar (InSAR) data, which provide high spatial resolution and near-field accuracy, have enabled detailed observations of coseismic deformation worldwide since 1992 (Massonnet et al., 1993; Elliott et al., 2016). Using InSAR analysis, numerous earthquakes have been mapped, and the resulting data have been used to constrain slip models. These InSAR-based source models provide detailed information on earthquake rupture and slip distribution (e.g., rupture location, depth, length, width, strike, dip, rake, and slip magnitude), and are widely regarded as independent estimates of seismic source parameters, commonly referred to as InSAR Centroid Moment Tensor (ICMT) solutions (Weston et al., 2011). Importantly, ICMT solutions provide constraints on the probable fault plane between the two nodal planes of seismic focal mechanisms (He et al., 2016). Nevertheless, ICMT source parameters are not consistently available for events in global catalogs (e.g., Barnhart et al., 2019; Luo et al., 2022), and are often buried in published tables (e.g., Elliott et al., 2010; Wang et al., 2014; He et al., 2020). Thus, the lack of a unified ICMT catalog limits our ability to characterize faulting patterns and their contribution to regional and global crustal deformation.

To investigate the role of N–S-trending rifts in accommodating crustal extension across the Tibetan Plateau, we compile refined catalogs of normal-faulting events from the ICMT and gWFM datasets. We construct a complete and internally consistent ICMT catalog (1992–present) by constraining finite-fault models with InSAR observations. We further refine the gWFM catalog (1976–present) by incorporating our synthetic body-waveform modeling results, and we assess its consistency with the ICMT solutions. The resulting normal-faulting events reveal spatial patterns and source characteristics that constrain the distribution of extensional deformation and the underlying tectonic dynamics of the Tibetan Plateau.

2. Tectonic Setting

The Tibetan Plateau spans about 2.5×10^6 km², with an average elevation of 5000 m and a crustal thickness exceeding 70 km, and was formed through the sequential accretion of crustal blocks during the northward subduction of the Indian plate (Tapponnier et al., 2001; Yin & Harrison, 2000; Taylor & Yin, 2009; Lu et al., 2018). From south to north, it comprises five major geological units: the Himalaya, Lhasa, Qiangtang, Songpan–Ganze, and Kunlun–Qaidam blocks, separated by suture zones (Figure 1). The plateau experiences strong N–S compression, E–W extension, rapid uplift, and high levels of seismic activity (Armijo, 1986; Huangfu et al., 2022; Shi et al., 2022; Li et al., 2022). Within the plateau, numerous small en echelon and V-shaped conjugate strike-slip faults accommodate E–W extension, indicating diffuse extensional deformation (Tapponnier & Molnar, 1976; Taylor et al., 2003; Blisniuk et al., 2001; Yang et al., 2009; Yin & Taylor, 2011).

Normal faults across the Tibetan Plateau, inferred from Landsat imagery, seismicity data, and field investigations, can be grouped into two distinct sets: E–W-trending faults of the South Tibetan Detachment System (STDS) and N–S-trending rifts that accommodate E–W extension (Searle et al., 2011). The STDS faults, confined to the southern Tibetan Plateau, result from N–S extension and shear and are characterized by low-angle, north-dipping faults that are generally inactive (Li et al., 2015). In contrast, the N–S-trending rifts, with geological slip rates of 1–4 mm/yr, represent the most significant active extensional structures in the Lhasa and Qiangtang blocks and are characterized by high seismic activity (Armijo et al., 1998; Searle et al., 2011; Figure 1). Thermochronological studies indicate that extension accommodated by these two fault types is coeval with the exhumation of the Himalayas (Thiede et al., 2009; Li et al., 2015).

In the southern Tibetan Plateau, which encompasses the Himalaya and Lhasa blocks, several major rifts are distributed from east to west, including the Cona, Yadong–Gulu, Pumqu–Xianza, Tangra–Yum Co, Xiakangjian, Thakkhola, Lunggar, Yagra, and Burang rifts. Further north, in the Qiangtang block, the principal rifts include the Amdo, Shuanghu, and Yutian rifts. These rifts are characterized by grabens (Ha et al., 2019), with typical spacings of 150–200 km and basin widths of several tens of kilometers (Kapp et al., 2008). Some rift systems extend across multiple blocks, with lengths of up to 500 km and depths of 300 km, potentially penetrating the full thickness of the lithosphere (Yin, 2000). Rift initiation dates to 18–13 Ma, marking the onset of plateau extension when the Tibetan Plateau had already reached more than 75% of its present elevation. This extension coincides with a change in horizontal deviatoric stress, from N–S compression ($\sigma_{ns} > \sigma_{ew} > \sigma_{zz}$, where σ denotes a principal stress) to E–W extension ($\sigma_{zz} > \sigma_{ns} > \sigma_{ew}$) (Masek et al., 1994; Williams et al., 2001; Lu et al., 2018).

3. Data and Methodology

To improve the accuracy and completeness of the normal-faulting catalog for the Tibetan Plateau, we collected primary seismological catalogs, SAR images, and teleseismic waveforms to produce our ICMT and gWFM catalogs. The ICMT catalog was constructed in two steps. First, SAR interferometric processing was used to detect surface deformation associated with normal-faulting events. Second, the resulting coseismic displacements were inverted using finite-fault models within a half-space elastic framework to determine fault geometry and slip distribution. The gWFM solutions are used to link the geodetic solution to the seismic solution, thereby enhancing the completeness of the normal-faulting event catalog.

3.1 SAR data and processing

We selected earthquakes with Mw ≥ 4.5 across the Tibetan Plateau from 1992 to the present. An initial dataset of approximately 200 events was compiled from the GCMT catalog and verified against the USGS and China Earthquake Administration (CEA) catalogs for completeness. This initial dataset did not distinguish fault types to avoid misclassification issues. For each event, we collected available C-band SAR images from the European Space Agency (ESA) satellites, including ERS-1/2, Envisat, and Sentinel-1, and derived coseismic interferograms using the GAMMA software (Wegnüller et al., 2016) to determine whether measurable surface deformation occurred. The 1-arcsec Shuttle Radar Topography Mission (SRTM) digital elevation model (DEM) was used to remove topographic phase contributions and for geocoding (Farr et al., 2007).

No events with Mw < 5.0 on the Tibetan Plateau produced detectable displacement signals above the noise level of the interferograms. As shown in Figure 1, approximately 120 events with Mw ≥ 5.0 occurred on and around the Tibetan Plateau, 78 of which have magnitudes between Mw 5.0 and 5.5. Due to the limited precision of source parameters from far-field waveform data, especially for earthquakes with Mw < 5.5, we reviewed each event on the Tibetan Plateau using InSAR observations. We excluded events that could be clearly identified as strike-slip earthquakes from the analysis, leaving 50 events with Mw ≥ 5.0 identified as normal faulting based on at least one line of evidence (seismological data, previous geodetic studies, or InSAR analysis). Details of the 50 retained normal-faulting events are listed in Supplementary Table S1. Given that significant incoherence occurred near the seismogenic fault of the 2008 Mw 7.1 Yutian event in C-band Envisat data, we used L-band SAR images to supplement coverage for source modeling. Noise levels in each interferogram were quantified using a 1D covariance-distance function (Parsons et al., 2005) and were typically 1–3 cm. Given the low signal-to-noise ratio (SNR), the 2017 Mw 5.2 Zhongba and 2021 Mw 5.6 Xainza events were excluded, leaving 26 events for geodetic source inversion using InSAR observations.

3.2 Finite-fault modeling

Finite-fault dislocation modeling is commonly used to characterize surface displacements associated with subsurface ruptures in an elastic half-space (Okada, 1985). In this study, we adopted a two-step inversion strategy to estimate the fault geometry and kinematic parameters. To reduce potential biases in the inversion, planar faults and robust inversion algorithms were used.

In the first step, a uniform-slip model (USM) was applied using the Geodetic Bayesian Inverse Software (GBIS; Bagnardi & Hooper, 2018). Using the USM, fault geometry (longitude, latitude, depth, width, length, strike, and dip) as well as the uniform slip vector (rake angle and slip magnitude) were determined. The Bayesian method is used to improve the robustness of USM estimates by considering both the model residuals and the posterior probability density of the source parameters. For normal-faulting events with simple surface deformation, a single fault was adopted, and its USM parameters were directly inverted without constraints. For the three events with complex ruptures (the 2008 Gerze sequence, 2008 Yutian, and 2008 Zhongba events), we used a two-segment fault model. In these cases, some fault geometry parameters (e.g., surface fault location, length, and strike) were fixed based on visual inspection of the InSAR deformation field, while the remaining parameters were inverted.

In the second step, on the basis of the fault structure identified by the USM, variable slip on each subpatch was inverted using the steepest descent method (SDM; Wang et al., 2009). To reduce edge effects, each fault plane was extended beyond the initial modeled rupture length and width, and subdivided into smaller subpatches with sizes of 2 km × 2 km or 1 km × 1 km. A Laplacian smoothing operator was applied to enforce spatial continuity of slip between adjacent subpatches. The optimal smoothing parameter was determined using an L-curve approach to balance data misfit and slip roughness.

3.3 Synthetic seismic body-waveform modeling

Seismological data were used to supplement the geodetic results as an independent constraint. Many earthquakes across the Tibetan Plateau have been studied seismologically in detail (e.g., Sloan et al., 2011; Craig et al., 2012). The gWFM catalog of Wimpenny and Watson (2021) documents most of these events over the past 50 years with Mw > 5.5 and many with Mw ≥ 5.0. We performed teleseismic body-wave modeling to determine the source properties of earthquakes studied with geodetic data in this work that lack prior detailed seismological analysis. Each earthquake was assumed to be represented by a single point-source (centroid), and modeling was conducted using the Grond software package of Heimann et al. (2019). For each earthquake, we determined the location (latitude, longitude, and depth), source duration, magnitude, and focal mechanism. We used both vertical-component data windowed around the direct P-wave and transverse-component data windowed around the S-wave arrival. In both cases, we used data windows designed to encompass both the direct arrival and its associated depth phases (pP, sP, sS), from 10 s before to 20 s after the predicted direct-phase arrival. Station response functions were removed from each trace and the data were filtered to between 0.06 and 1.0 Hz. During the inversion process, we downweighted misfits from the transverse-component data by a factor of two to compensate for the usually higher amplitudes of the S-wave and its depth phases. At each iteration of the inversion, we allowed a time shift that maximized the cross-correlation between the synthetic and observed waveforms for each trace.

To allow comparison with our geodetic results, we inverted for a focal mechanism constrained to be purely double-couple, equivalent to slip on a discrete plane as in our geodetic inversion. We also inverted for a deviatoric moment tensor, which permits a non-double-couple component likely representing either non-planar source complexities or the mapping of noise into the mechanism. In either case, the match between the double couple and deviatoric moment tensors offers a qualitative metric for identifying poorly determined mechanisms from the seismological data. Our seismological inversions determined a lateral location shift relative to an initial location estimate. However, we note that teleseismic data depart from the earthquake source at high take-off angles, and that comparatively low frequencies were used. As a result, the resolution possible in lateral location is poor, especially in comparison to the constraints provided by geodetic data. In contrast, depth is better constrained by these teleseismic data owing to the steep take-off angles and the inclusion of depth phases.

4. Results

4.1 ICMT catalog

We identify 28 events with detectable InSAR deformation, distributed in six regions (A–F) within the Tibetan Plateau region (Figure 1). Among these 28 events, three earthquake sequences are identified: the 1998 Pumqu–Xianza, 2008 Gerze, and 2016 Dinggye sequences (Supplementary Table S3). Owing to the limited temporal resolution of InSAR observations, each earthquake sequence appears as a single event in the interferograms, making it difficult to separate coseismic deformation from individual subevents. Accordingly, these sequences are treated as single events. Figure 2 presents the local tectonic setting and coseismic displacement results for normal-faulting events in one of these regions. Detailed interferogram information for all identified normal-faulting events is provided in Supplementary Figures S1–S6 and Tables S1–S2.

Except for the 2025 Tingri event, coseismic displacements for all other events are no more than 50 cm, with most less than 10 cm. Two events show only minor displacements within ± 1 cm: the 2017 Mw 5.2 Zhongba event and the 2021 Mw 5.6 Xainza event. These interferograms indicate that all events are associated with geologically active rifts. No surface ruptures were identified, except for the 2008 Mw 7.1 Yutian and 2025 Mw 7.0 Tingri events. Coseismic deformation surface patterns for the 1994 Mw 5.9 Baqen and 2021 Mw 5.6 Xainza events are reported here for the first time (Supplementary Table S1). Additionally, four events (the 2003 Mw 5.8 Shuanghu, 2004 Mw 6.1 Shuanghu, 2007 Mw 6.0 Rutog, and 2008 Mw 5.8 Zhongba events) are interpreted as normal faulting based on the interferograms; this contrasts with the strike-slip focal mechanisms reported by the GCMT catalog. Furthermore, the 2015 Mw 5.9 Tingri event, not listed in the

GCMT catalog but included in the CEA catalog, is interpreted as a normal-faulting event on the basis of interferogram analysis.

Our USM results indicate that these normal-faulting events can be effectively modeled using either a single-segment fault or, for more complex ruptures, a two-segment configuration (Supplementary Figures S7–S60 and Table S3). Bayesian inversion results indicate that most fault geometries are constrained within 2σ uncertainties of ± 3 km for length, ± 4 km for width, ± 2 km for depth, ± 10° for dip angle, ± 10° for strike angle, ± 15° for rake angle, and ± 3 km for horizontal location (X and Y). Large uncertainties in source model parameters primarily occur for events with low-SNR in the observations, including the 1992 Nyemo, 1994 Baqen, 2015 Tingri, and 2021 Biru events. In addition, when deformation patterns are subtle and only a single radar line-of-sight (LOS) geometry is available, InSAR constraints can be significantly limited, as in the 2004 Shuanghu event. By contrast, results for other events show much smaller uncertainties in fault geometry parameters, e.g., ± 3° for dip angle, ± 2° for strike angle, respectively. The USM results comprise 27 models for 26 events, with the additional model corresponding to the 2018 Gerze sequence, whose two-segment fault represents both the mainshock and its largest aftershock (Mw 5.8). These results demonstrate the capability of InSAR to resolve shallow normal-faulting events on the Tibetan Plateau, including complex sequences with multiple rupture segments.

On the basis of the USM-derived fault geometry, the DSM results reveal detailed slip characteristics, including rupture dimensions, depths, and asperity patterns. Examples of slip distributions are shown in Figure 3. The full set of slip distributions is provided in Supplementary Figures S61–S66 and Table S3. Except for these three events (the 2008 Yutian, 2008 Zhongba sequence, and 2025 Tingri events), peak slip for the remaining events generally ranges from 0.3 to 1 m, with rupture areas ranging in size from 6 km in length × 6 km in width to 20 km in length × 20 km in width. They are typically concentrated in a single asperity at depths shallower than 12 km, exhibiting an approximately circular shape, although fine-scale details cannot be resolved due to the model resolution and smoothing constraints. In addition, these events are characterized by shallow rupture, with slip generally not reaching the surface except for the 2018 Yutian and 2025 Tingri events. DSM fits to the observed displacements for these events are provided in Supplementary Figures S67–S92.

4.2 Body-waveform modeling results

Figure 4 and Supplementary Figures S90–S91 present the moment tensor solutions and depths for each event, along with four example waveforms and corresponding best-fitting synthetics. Supplementary Table S4 lists the source models of the fourteen earthquakes for which geodetic results are presented. Of these, eleven yield stable inversion results, while three have insufficient data for reliable inversion. All events studied here have shallow sources (centroid depths < 10 ± 2 km), reflecting the limited depth range accessible with geodetic rather than seismic data.

4.3 Comparison between the ICMT and gWFM catalogs and their relation to earlier seismological catalogs

The final compilations of normal-faulting events from the ICMT and gWFM catalogs is shown in Figure 5. Our ICMT catalog contains source models of 26 events since 1992, including locations, coseismic displacements, well-constrained fault geometries, and slip distributions. As shown in Figure 5a, events in the

ICMT catalog have magnitudes ranging from Mw 5.2 to 7.1, with the majority being Mw ≥ 5.5 and only three in the magnitude range of Mw 5.0 to 5.5. Depths of peak slip are all shallower than 10 km, and primary rupture widths increase gradually with magnitude. By contrast, the gWFM catalog comprises 36 events from 1976 to the present, including 25 from the published catalog (Wimpenny and Watson, 2021) and 11 newly determined in this study. The gWFM catalog provides solutions for the two nodal planes of each event (one of which is the true fault plane), but does not include rupture dimensions or detailed slip distributions. As shown in Figure 5b, the gWFM catalog includes several additional events with Mw < 5.5, while all events have centroid depths shallower than 12 km. The two catalogs share 24 overlapping events. Three events (the 2004 Mw 5.2 Shuanghu, 2015 Mw 5.9 Tingri, and 2016 Mw 5.3 Dinggye events) are present in the ICMT catalog but absent from the gWFM results. Thirteen events are present only in the gWFM catalog, with 10 occurring before 1992. This indicates good temporal complementarity between the two catalogs.

In addition, we compare source parameters between the two catalogs, including longitude, latitude, depth, strike, dip, rake, and magnitude. For the ICMT catalog, the longitude, latitude, strike, dip, and rake parameters are from the USM solutions, and the depth and magnitude are from the DSM solutions. We calculate the moment-weighted center of the fault slip patch as the geodetic centroid depth for the ICMT catalog cases (Supplementary Figure S95). For the gWFM catalog, we consider only the nodal plane that corresponds to the ICMT catalog for comparison. The source models in the two catalogs show good agreement (Supplementary Figure S96). Importantly, both catalogs support shallow ruptures of normal-faulting earthquakes in the Tibetan Plateau interior (Figure 5c).

Earlier seismological catalogs (e.g., GCMT, USGS, and CEA; Supplementary Tables S3–S4) provide the initial event locations, magnitudes, and focal mechanisms for constructing our ICMT and updated gWFM catalogs. However, these catalogs may include focal mechanism misclassifications, omit relatively small shallow events, and generally report only centroid depths (10–25 km), which are less reliable for normal-faulting earthquakes on the Tibetan Plateau. The gWFM catalog improves upon these datasets by providing a consistently determined set of focal mechanisms and more reliable source depths (Wimpenny & Watson, 2021). Our ICMT catalog incorporates InSAR-derived coseismic displacement fields and finite-fault modeling, resolving fault geometries and spatial slip distributions in detail. These advances enable robust assessments of rupture scaling, the depth distribution, and the mechanics of normal-faulting earthquakes, providing clear insight into regional extensional tectonics. As normal-faulting earthquakes with Mw < 5.0 produce little or no detectable coseismic deformation in InSAR data, and events with Mw 5.0–5.5 often have low SNR, the ICMT catalog includes only events with Mw ≥ 5.5.

4.4 Scaling properties of normal-faulting events

Our ICMT catalog characterizes the scaling properties of normal-faulting earthquakes on the Tibetan Plateau. Rupture dimensions are relatively compact (Figure 6a). Most events have widths of < 20 ± 4 km and lengths of < 25 ± 3 km. Smaller events typically rupture a single fault segment, whereas larger events (Mw > 6.5; e.g., the 2008 Mw 7.1 Yutian, 2008 Mw 6.6 Zhongba, and 2025 Mw 7.0 Tingri earthquakes) often involve two connected segments, producing rupture lengths of up to about 50 km. Rupture width-to-length ratios range from 0.36 to 1.7, with a mean of 0.8, consistent with a nearly circular rupture geometry. Such compact scaling is likely controlled by the limited seismogenic thickness of the plateau crust and reflects the influence of a relatively uniform extensional stress field.

Stress drop $\Delta\sigma$is calculated following Cocco et al. (2016),

$$\Delta\sigma = \frac{7}{16}\frac{M_0}{A^{3/2}} \qquad (1)$$

where M_0 is the seismic moment and A is the fault rupture area. All stress drops for the analyzed normal-faulting events are < 1 MPa (Figure 6b), which lies at the lower end of the broad range of observed stress drops (0.1–100 MPa; Hecker et al., 2010; Cocco et al., 2016). Such uniformly low stress drops suggest that the normal-faulting earthquakes occurred under a relatively weak stress environment, potentially reflecting slip along mature fault segments. This contrasts with previous studies, which suggest that higher stress-drop earthquakes tend to occur on relatively immature faults (Hecker et al., 2010).

We observe a log-linear relationship between earthquake magnitude (Mw) and rupture length (L), in agreement with previous studies (Wells & Coppersmith, 1994; Leonard, 2010; Schirripa Spagnolo et al., 2021):

$$Mw = \mathrm{a} + \mathrm{b} \cdot \log(L) \qquad (2)$$

where a and b are the model coefficients. Compared with previous studies, our model yields smaller coefficients and provides a better description of rupture characteristics for the Tibetan Plateau (Figure 6c). In addition, log-linear relationships are estimated between earthquake magnitude and other rupture parameters, including the average slip, width, and rupture area (Supplementary Figure S97). These distinctive scaling coefficients may reflect the unique extensional deformation regime of normal-faulting earthquakes in the Tibetan Plateau region.

5. Discussion

5.1 Dip angles of normal faults and extensional tectonic implications

In extensional tectonics, the variation in dip angles of normal-faulting earthquakes reflects different stages of fault evolution, which are associated with differences in geometry, formation mechanisms, activity modes, and seismic behavior (Kapp et al., 2008). In other words, variations in fault dip angles may reflect extensional structures of different ages. On the basis of this assumption, two extensional patterns have been proposed to explain and predict the Tibetan Plateau extension. The first involves gravitational collapse-driven extension, inferred from the initiation ages of rifts (Figure 7a). Geochronological data (e.g., ^{40}Ar–^{39}Ar, (U-Th)/He, and Th-Pb) indicate that the initiation ages of N–S-trending rifts span 23–2.8 Ma (e.g., Blisniuk et al., 2001; Kapp et al., 2005, 2008; Ratschbacher et al., 2011; Styron et al., 2013, 2015; Wolff et al., 2019; Bian et al., 2020, 2022). The west-to-east decrease in initiation ages of the N–S-trending rifts suggests a sequential gravitational collapse-driven pattern, in which fault dip angles vary systematically across the plateau from west to east (Cooper et al., 2015; Li et al., 2015; Bian et al., 2022).

An alternative hypothesis is that normal faults across the plateau exhibit approximate axial symmetry due to the curvature of the Himalayan arc, which resolves subduction-related motion of the Indian plate into along-strike components (Wolff et al., 2019). Based on topography, field geology, and seismological data, previous studies estimate dip angles of N–S-trending rifts across the plateau as ranging from 10° to 70° (Figure 7b) (e.g., Kapp et al., 2005, 2008; Ratschbacher et al., 2011; Wolff et al., 2019; Chevalier et al., 2020). These dip angles indicate that high-angle normal faults are concentrated near a symmetry axis at ∼87°E, while low-angle faults occur farther to the west and east. This spatial pattern is consistent with an increase in the arc-parallel component of the India–Asia convergence vector, supporting the oblique-convergence model (Styron et al., 2011; Wolff et al., 2019).

To compare these two extension patterns on the Tibetan Plateau, the dip angles of normal-faulting events from our ICMT catalog are shown in Figure 7a–b. The normal-faulting events exhibit various dip angles, and their distribution does not support either a west-to-east sequential pattern or an axial pattern centered at 87°E. The discrepancy partly arises from geological dip estimates reflecting the long-term architecture of rift systems, whereas ICMT-derived dip angles reflect coseismic slip on localized fault planes. To reconcile geological and geodetic observations, we suggest that the distribution of normal-faulting dip angles reflects a transition from early-stage development of large-scale rift systems to a later stage of local structural adjustment within each rift. Most earthquakes in our catalog are associated with rifts that initiated between 13 and 16 Ma, with few events on older (> 16 Ma) or younger (< 10 Ma) rifts (Figure 7c).

An important question is whether normal-faulting earthquake occurrence is controlled by the corresponding dip angle (e.g., Wernicke, 1995; Collettini, 2011; Styron & Hetland, 2014). High-angle normal faults characterize immature basins and typically occur in the shallow crust. They are more active and likely to generate earthquakes. In contrast, low-angle normal faults (LANFs; dip angle of < 35°) shape mature basins and often involve deeper structural processes. They are less active and may not produce shallow seismicity (Kapp et al., 2008). Active normal-faulting structures associated with LANFs are common in geological records, such as low-angle, core-complex domes in the northern Snake Range, USA, and the Alps, Europe (Wrobel et al., 2021). Indeed, continental normal-faulting earthquakes are rarely observed on LANFs or on very high-angle faults (> 65°) (Abers, 1991, 2001; Abers et al., 1997), but generally occur on faults with intermediate dip angles (35°–65°) (e.g., Jackson et al., 1989; Cogan et al., 1998; Elliott et al., 2010). In this study, approximately 80% of the normal-faulting events exhibit intermediate dip angles, but one low-angle (< 35°) and six high-angle (> 65°) events were also detected (Figure 7d). The 2018 Xietongmen Mw 5.6 event, with a low-angle dip of 24 ± 10.0°, is the only notable exception to the idea that LANFs are generally seismically inactive. Of the six very high-angle (>65°) events, five have dip angles between 65° and 70°. The 2003 Shuanghu Mw 5.8 event has an exceptionally steep dip of 89 +1/-6°. A detailed analysis is provided in Supplementary Figures S98–S100 and Text S2. Note that events with unusually low or very high dip angles may result from high uncertainties in the datasets and thus could represent measurement noise. Alternatively, they may reflect true structural heterogeneity, oblique reactivation along pre-existing fabrics, or depth-dependent stress variations (Yin & Taylor, 2011), all of which require further investigation. Nevertheless, these events represent only a small fraction of the catalog and do not significantly affect the regional dip-angle statistics, scaling relationships, or strain-budget estimates presented here. Overall, our results support the idea that low-angle (< 35°) normal faults along the rifts are generally seismically inactive, although they may accommodate aseismic deformation. In contrast, the occurrence of high-angle normal-faulting events suggests that new extensional structures continue to develop in the plateau interior.

5.2 Normal-faulting events related to topography and crustal thinning

Understanding how the extreme elevation of the Tibetan Plateau affects the occurrence of normal-faulting earthquakes is important for exploring regional tectonic stress, crustal thinning, gravitational potential energy and earthquake hazards (Elliott et al., 2010; Fang et al., 2024). Molnar et al. (1993) and Elliott et al. (2010) examined normal-faulting events from the GCMT catalog at elevations of 4000 m and 4500 m, respectively, to explore the extensional tectonics of the Tibetan Plateau. Furthermore, Elliott et al. (2010) defined significant moment release in normal-faulting earthquakes as occurring at elevations above 4750 m. Zheng et al. (2017) calculated strain in the India–Eurasia collision zone using 25 years of Global Navigation Satellite System (GNSS) observations, showing that significant dilatation occurred mainly at elevations above 4750 m.

Compared with previous studies (e.g., Elliott et al., 2010), our results incorporate an additional 15 years of data. This extension allows a longer catalog period and provides detailed source models, improving overall completeness. On the basis of the updated catalog, we compared the relationship between normal-faulting events and high topography (Figure 8a). Normal-faulting earthquakes predominantly occur at elevations of 4400–6100 m, with 70% occurring above 5000 m. The largest events, the 2008 Mw 7.1 Yutian event and the 2025 Mw 7.0 Tingri event, occurred at elevations of 5800 m and 4500 m, respectively.

Geodetic measurements indicate significant extensional deformation in the Tibetan Plateau area, resulting in high geodetic strain and notable crustal thinning along E20°S (Zhang et al., 2004; Zheng et al., 2017; Wright et al., 2026). This raises the question of whether these geodetic strains are accommodated by the normal-faulting events. Theoretically, the accumulated scalar moments within the seismogenic zone should correspond to the accumulated surface strain (Kostrov, 1974; Savage & Simpson, 1997). As the moments of normal-faulting events are related to the vertical (thinning) strain rate, their relationship can be described as follows (Kostrov, 1974; Elliott et al., 2010),

$$\dot{\varepsilon_{ij}} = \frac{1}{2\mu Vt}\sum_n M_{ij}^n = \frac{1}{2\mu HAt}\sum_n M_{ij}^n \qquad (3)$$

where $\dot{\varepsilon_{ij}}$ is the ijth component of the strain-rate tensor, $\sum_n M_{ij}^n$ is the sum of the moment tensors of n earthquakes within a volume V over a time interval t, and μ is the shear modulus. The volume V is defined as the product of the seismogenic zone thickness H and area A. Assuming negligible volumetric strain over long timescales, the average vertical strain of the Tibetan Plateau is estimated to be -5×10^{-9} yr^{-1}, based on a horizontal extensional strain of $2.1 \pm 0.3 \times 10^{-8}$ yr^{-1} and a contractional strain of $-1.6 \pm 0.4 \times 10^{-8}$ yr^{-1} derived from GNSS observations (Zhang et al., 2004; Elliott et al., 2010). Using the GCMT catalog, Elliott et al. (2010)

estimated that a total moment of 1.4×10^{20} N·m was released over a 43-year period across the plateau. On the basis of the released moment, they calculated the thinning strain rate over an area of 2.0×10^{6} km² (elevation above 4200 m), resulting in 1.7×10^{-9} yr^{-1} for a seismogenic layer thickness of 15 km, or 2.6×10^{-9} yr^{-1} for a thickness of 10 km ($\mu = 3.23 \times 10^{10} Pa$ in all calculations). This implies that the normal-faulting events account for only 30%–50% of the total vertical strain rate.

In this study, the total seismic moment of the normal-faulting events in the ICMT and gWFM catalogs is $1.55 \pm 0.04 \times 10^{20}$ N·m over the past 49 years (since 1976) (Supplementary Figure S101). Compared with the GCMT catalog used by Elliott et al. (2010), our updated catalog excludes normal-faulting events associated with deep subduction and incorporates more recent normal-faulting events, including the large 2025 Tingri event. In addition, our results suggest a seismogenic thickness of approximately 12 km. For comparison, we calculate the thinning strain rate using the updated seismogenic thickness and moment release from this study, together with the area suggested by Elliott et al. (2010). The vertical moment tensor component of the normal-faulting events in our catalog is 1.3×10^{20} N·m, corresponding to a thinning strain rate of 2.1×10^{-9} yr^{-1}, equivalent to 42% of the GNSS-derived vertical strain rate (5×10^{-9} yr^{-1}).

Moreover, we perform a similar strain rate analysis using 1-km-resolution large-scale interseismic InSAR observations (Wright et al., 2026) and calculate the dilation strain rate in the region of normal-faulting events (Figure 8b). These normal-faulting events cover a surface area of 1.1×10^{6} km^{2}, approximately half of that estimated by Elliott et al. (2010), due to differences in the spatial definition of the study region in our catalog. Considering the sum of the horizontal moment tensor components of $1.3 \pm 0.1 \times 10^{20}$ N·m from seismicity in this region, we estimate the dilatational strain rate to be $3.2 \pm 0.2 \times 10^{-9}$ yr^{-1}. Notably, the uncertainties of earthquake moment tensors are difficult to quantify; here, we approximate them by evaluating the slip perturbations caused by geodetic observation errors.

On the other hand, the geodetic rate of surface area increase for this region is 4.7×10^{-3} km^2/yr, corresponding to an average geodetic dilatational strain rate of 4.3×10^{-9} yr^{-1}. The uncertainty of the regional mean interseismic dilatational strain rate is estimated to be less than 1×10^{-9} yr^{-1}, based on the uncertainty reported by Wright et al. (2026) and standard error propagation. That is, the dilatational strain rate associated with seismicity is 74% ± 5% of the interseismic geodetic dilatational strain rate. The Yutian region (outlined in green in Figure 8b) is in the northwestern Tibetan Plateau, far from the plateau interior (outlined in pink). It has experienced a series of large events, including the 2008 Mw 7.1 Yutian event, the 2020 Mw 6.3 event, and several strike-slip events over the past two decades. We also consider the Yutian region alone and calculate the strain as described above. The Yutian region covers approximately 6.1×10^4 km^2. The associated seismic moment corresponds to a dilatational strain rate of $2.2 \pm 0.2 \times 10^{-8}$ yr^{-1}, equivalent to about 85% ± 8% of the average geodetic dilatational strain rate (2.6×10^{-8} yr^{-1}). Excluding the Yutian region, the plateau interior covers 1.0×10^6 km^2. The associated seismic moment corresponds to a dilatational strain rate of $2.1 \pm 0.2 \times 10^{-9}$ yr^{-1}, equivalent to approximately 72% ± 7% of the average geodetic dilatational strain rate (2.9×10^{-9} yr^{-1}). Considering that earthquakes with Mw < 5.0, which are not included in our ICMT and gWFM catalogs, contribute an additional 10% of the total released seismic moment (Scholz and Cowie, 1990), accounting for this contribution, we estimate that the Yutian region and the plateau interior released seismic moments equivalent to 95% ± 8% and 82% ± 7% of the total geodetic dilatational strain rate, respectively. This implies that the remaining geodetic dilatational strain rate deficits are 5% ± 8% and 18% ± 7%, respectively. Assuming the short-term geodetic strain represents long-term earthquake hazards, the remaining 18% ± 7% geodetic dilatational strain rate deficit in the plateau interior is equivalent to a Mw 6.9 ± 0.1 normal-faulting event or may be accommodated by aseismic deformation.

Specifically, these strain rates primarily reflect the integrated deformation within the upper seismogenic crust, and do not necessarily imply net crustal thinning at the lithospheric scale. Numerous geophysical studies indicate substantial underthrusting of the Indian lithosphere and lower-crustal inflow beneath the plateau, contributing to ongoing crustal thickening at depth (Yin & Taylor, 2011; Styron et al., 2015; Taylor et al., 2021). Within this geodynamic framework, upper-crustal extension represents the shallow expression of deeper lithospheric mass redistribution rather than a purely upper-crust–driven thinning process. Accordingly, our results provide quantitative constraints on how the shallow crust responds to deeper lithospheric dynamics, thereby improving our understanding of lithospheric decoupling.

5.3 Distribution of normal-faulting events and gravitational potential energy

Normal-faulting events on the Tibetan Plateau are concentrated within a confined region bounded by the Himalayan arc to the south and the Kunlun–Manyi fault (i.e., Jinsha Jiang suture) to the north. They are largely absent from both the eastern and western tectonic syntaxes (Figure 8b). Tomography and earthquake-depth observations reveal that the Indian plate subducts northward beneath the Tibetan Plateau at a gentle dip angle (Galetzka et al., 2015; Zhang et al., 2023), with its northern edge reaching the Jinsha Jiang suture zone (Chen et al., 2017; Wolff et al., 2023). Along this northern boundary, a series of large strike-slip events have been documented, such as the 1997 Mw 7.6 Manyi event (Funning et al., 2007), the 2001 Mw 7.8 Kokoxili event

(Lasserre et al., 2005), and the 2021 Mw 7.4 Maduo event (Fang et al., 2022). On the other hand, the northward subduction of the Indian slab exhibits a steep dip angle along its eastern and western sides, as indicated by deep-focus earthquakes with depths of up to 300 km in the Hindu Kush and Burmese Arc (Craig et al., 2012, 2020). The eastern and western tectonic syntaxes effectively bound the extension domain. Consistent with this geometry, the spatial distribution of normal-faulting events broadly correlates with variations in the architecture of the Indian slab. However, further evidence is needed to better constrain their linkage.

Our catalog of normal-faulting events demonstrates that rupture occurs predominantly within a shallow seismogenic layer at depths shallower than 12 km. Previous postseismic studies indicate that afterslip is largely confined to the upper crust (< 15 km) (Ryder et al., 2010; Hong et al., 2023), whereas viscoelastic relaxation with relatively low viscosity occurs in the lower crust (Wen et al., 2012). This behavior is consistent with geophysical evidence suggesting a mechanically weak and ductile lower crust beneath the plateau (Shin et al., 2022; McMillan & Schoenbohm, 2023). The China Seismological Reference Model (CSRM-1.0) reveals a large-scale low-velocity layer at a depth of 40 km between the downward-moving Indian Plate and the overlying Tibetan crust (Xiao et al., 2024). Furthermore, high-conductivity anomalies have been detected at depths of 25–65 km beneath the graben systems in the Lhasa and Qiangtang blocks, implying a hot, low-viscosity mid-to-lower crustal layer (Tian et al., 2015; Dong et al., 2020). This weak lower crust provides a decoupled environment in which brittle deformation is concentrated in the upper crust. As a result, seismicity across the plateau is predominantly confined to depths < 20 km, with normal-faulting events typically limited to < 12 km depth. This depth range corresponds to the inferred seismic–aseismic transition, which coincides with the 350°C isotherm based on thermal modeling and geological constraints (Craig et al., 2012, 2020). Magnetotelluric studies further support this interpretation, indicating a resistive upper crustal layer approximately 10–15 km thick (Alsdorf & Nelson, 1999). Collectively, these observations support a model in which normal-faulting earthquakes within the plateau are accommodated entirely within a shallow, brittle upper crust decoupled from the underlying hot, weak lower crust.

The coexistence of relatively low stress drops, segment-limited rupture dimensions, and shallow rupture depths is consistent with a thermally weakened and mechanically stratified lithosphere beneath the Tibetan Plateau. Elevated geothermal gradients and a weak, ductile lower crust may reduce the effective lithospheric strength and promote distributed deformation at depth, thereby limiting rupture propagation to the brittle upper crust and favoring segmented faulting (Bischoff & Flesch, 2018; Craig et al., 2012, 2020; Shin et al., 2022). In this framework, normal faults across the plateau likely reflect deformation within a warm, thickened crust characterized by strong rheological layering (Taylor et al., 2003, 2021; Taylor & Yin, 2009) rather than extension in a cold and mechanically homogeneous lithosphere.

Gravitational potential energy (GPE) associated with the extreme topography and thick crust is widely considered the primary driver of crustal extension and thinning (e.g., Bischoff & Flesch, 2018, 2019; Jay et al., 2018; Fang et al., 2024). The Tibetan Plateau shows an average Moho depth of 65 km based on the Crust 1.0 model (Laske et al., 2013) (Figure 9a). Normal-faulting events are primarily located in areas with significant crustal thickness gradients across the plateau. Some thick-crust areas, such as the West Kunlun and the Karakorum region, do not host normal-faulting events. Assuming isostatic balance of the present-day topography, Fang et al. (2024) estimated the gravitational potential energy (GPE) based on a uniform lithospheric structure down to 100 km depth and considered slip resistance on major lithospheric-scale faults.

Using this model, they predicted the distribution of active faulting types in the Tibetan Plateau (Figure 9b). We find that the distribution of normal-faulting events in our catalog closely matches the model-predicted regions of normal faulting (i.e., NS and NN in Figure 9b). This pattern reflects a balance between boundary forces and GPE-driven internal buoyancy forces. Therefore, the spatial distribution of normal-faulting events is strongly associated with high topography, thick crust, and the interplay between boundary forces and internal buoyancy, which are further modulated by lithospheric-scale faults.

6. Conclusion

In this study, using InSAR and gWFM data, we compile a multidecadal catalog of normal-faulting earthquakes on the Tibetan Plateau. Our catalog indicates that normal-faulting activity is primarily concentrated at shallow depths (< 12 km), and earthquake rupture lengths and widths are broadly comparable. This geometric characteristic is consistent with single-segment ruptures being limited to Mw < 6.5, whereas three events with Mw > 6.5 (i.e., the 2008 Mw 7.1 Yutian, 2008 Mw 6.6 Zhongba, and 2025 Mw 7.0 Tingri events) ruptured two segments. Across the plateau, intermediate- and high-angle faults dominate, with the 2018 Xietongmen earthquake as the only potential exception. The dip angles of the events exhibit significant spatial and temporal variability, suggesting that extensional tectonics across the plateau evolved in multiple stages rather than following a simple symmetrical or west-to-east sequential pattern. Additionally, approximately 85% of the geodetic dilatational strain is accommodated by seismicity. The remaining strain may reflect aseismic processes, such as afterslip, which require further investigation.

Declaration of Competing Interest

The authors acknowledge that there are no conflicts of interest recorded.

Data Availability Statement

The GBIS code (Bagnardi & Hooper, 2018) used for the uniform slip inversion modeling in the study is available at the COMET website: https://comet.nerc.ac.uk/geodetic-bayesian-inversion-software-gbis. The SDM code (Wang et al., 2009) used for the distributed slip inversion modeling is available on GitHub: https://github.com/RongjiangWang/SDM. All C-band SAR data were provided by the ESA through their open data policy and can be accessed via the Alaska Satellite Facility (ASF): https://search.asf.alaska.edu. The earthquake catalogs used in this study are available from the U.S. Geological Survey (USGS): https://earthquake.usgs.gov/earthquakes, the Global Centroid Moment Tensor (GCMT) catalog: https://www.globalcmt.org, and the China Earthquake Networks Center (CENC): https://data.earthquake.cn. The published gWFM catalog cited in this study was published by Wimpenny and Watson (2021): https://github.com/samwimpenny/Global-Waveform-Catalogue. Figures were plotted using Generic Mapping Tools (GMT): https://www.generic-mapping-tools.org.

Acknowledgments

We sincerely thank Editor Anke Friedrich and the Associate Editor for handling our manuscript and providing helpful guidance. We also thank the reviewers, Professors Jeff Freymueller and Michael H. Taylor, for their constructive suggestions. We are grateful to Professors Greg Houseman, Alex Copley, Jing Liu-Zeng, Dr. Qi Ou, and Dr. Shaozhuo Liu for insightful discussions that greatly improved the manuscript, and to Professor Weipeng Ge for providing the locations of rifts. This work was supported by the National Natural Science Foundation of China (42174004 and 42374003). COMET is the UK NERC Centre for the Observation and Modeling of Earthquakes, Volcanoes and Tectonics, a partnership between UK universities and the British

Geological Survey. Ping He is an academic visitor at the University of Leeds, sponsored by the State Scholarship Fund from the China Scholarship Council. Tim Craig was supported in this work by the Royal Society under URF/R1/180088 and URF/R/231019. John Elliott is supported by the Royal Society through a University Research Fellowship (URF/R/211006). Figures were plotted using Generic Mapping Tools (GMT). OpenAI ChatGPT (GPT-5.3) was used to check spelling and grammar errors throughout the manuscript.

Open Research

The GBIS code used for the uniform slip inversion modeling is available at (Bagnardi & Hooper, 2018).

The SDM code used for the distributed slip inversion modeling is available at (Wang et al., 2009).

The SAR datasets were provided by the European Space Agency (ESA) and accessed through the ASF Distributed Active Archive Center (DAAC), NASA EOSDIS (Alaska Satellite Facility, 2025).

The earthquake catalog datasets used in this research can be accessed from the USGS (USGS, 2025); the GCMT (Ekström et al., 2012); and the CENC (CENC, 2025) websites.

The published gWFM catalog dataset referenced in this study is available at (Wimpenny & Watson, 2021).

Reference

Abers, G. A. (1991). Possible seismogenic shallow-dipping normal faults in the Woodlark-D'Entrecasteaux extensional province, Papua New Guinea. *Geology, 19(12)*, 1205–1208. https://doi.org/10.1130/0091-7613(1991)019<1205:PSSDNF>2.3.CO;2

Abers, G. A. (2001). Evidence for seismogenic normal faults at shallow dips in continental rifts. *Geological Society, London, Special Publications, 187(1)*, 305–318. https://doi.org/10.1144/GSL.SP.2001.187.01.1

Abers, G. A., Mutter, C. Z., & Fang, J. (1997). Shallow dips of normal faults during rapid extension: Earthquakes in the Woodlark-D'Entrecasteaux rift system, Papua New Guinea. *Journal of Geophysical Research: Solid Earth, 102(B7)*, 15301–15317. https://doi.org/10.1029/97JB00787

Alaska Satellite Facility. (2025). ASF DAAC Data Search. NASA EOSDIS [Dataset]. https://search.asf.alaska.edu/, last accessed 21 November 2025.

Alsdorf, D., & Nelson, D. (1999). Tibetan satellite magnetic low: evidence for widespread melt in the Tibetan crust? *Geology, 27(10)*, 943–946. https://doi.org/10.1130/0091-7613(1999)027<0943:TSMLEF>2.3.CO;2

Armijo, R., Tapponnier, P., Mercier, J. L., & Han, T. L. (1986). Quaternary extension in southern Tibet: Field observations and tectonic implications. *Journal of Geophysical Research: Solid Earth, 91(B14)*, 13803–13872. https://doi.org/10.1029/JB091iB14p13803

Bagnardi, M., & Hooper, A. (2018). Inversion of surface deformation data for rapid estimates of source parameters and uncertainties: A Bayesian approach [Software]. *Geochemistry, Geophysics, Geosystems, 19(7)*, 2194–2211. https://doi.org/10.1029/2018GC007585

Barnhart, W. D., Hayes, G. P., & Wald, D. J. (2019). Global earthquake response with imaging geodesy: Recent examples from the USGS NEIC. *Remote Sensing, 11(11)*, 1357. https://doi.org/10.3390/rs11111357

Bian, S., Gong, J., Zuza, A. V., Yang, R., Chen, L., Ji, J., et al. (2022). Along-strike variation in the initiation timing of the north-trending rifts in southern Tibet as revealed from the Yadong-Gulu rift. *Tectonics, 41(7)*, e2021TC007091. https://doi.org/10.1029/2021TC007091

Bian, S., Gong, J., Zuza, A. V., Yang, R., Tian, Y., Ji, J., et al. (2020). Late Pliocene onset of the Cona rift, eastern Himalaya, confirms eastward propagation of extension in Himalayan–Tibetan orogen. *Earth and Planetary Science Letters, 544*, 116383. https://doi.org/10.1016/j.epsl.2020.116383

Bird, P. (1979). Continental delamination and the Colorado Plateau. *Journal of Geophysical Research: Solid Earth, 84(B13)*, 7561-7571. https://doi.org/10.1029/JB084iB13p07561

Bischoff, S. H., & Flesch, L. M. (2018). Normal faulting and viscous buckling in the Tibetan Plateau induced by a weak lower crust. *Nature Communications, 9(1)*, 4952. https://doi.org/10.1038/s41467-018-07312-9

Bischoff, S., & Flesch, L. (2019). Impact of lithospheric strength distribution on India–Eurasia deformation from 3-D geodynamic models. *Journal of Geophysical Research: Solid Earth, 124*, 1084–1105. https://doi.org/10.1029/2018JB015704

Blisniuk, P. M., Hacker, B. R., Glodny, J., Ratschbacher, L., Bi, S., Wu, Z., et al. (2001). Normal faulting in central Tibet since at least 13.5 Myr ago. *Nature, 412(6847)*, 628–632. https://doi.org/10.1038/35088045

Blom, N., Hardalupas, P. S., & Rawlinson, N. (2023). Mitigating the effect of errors in source parameters on seismic (waveform) tomography. *Geophysical Journal International,* 232(2), 810–828. https://doi.org/10.1093/gji/ggac314

CENC. 2025. The Chinese National Earthquake Data Center [Dataset]. https://data.earthquake.cn/, last accessed 21 November 2025.

Chen, H., Qu, C., Zhao, D., Shan, X., Li, C., & Dal Zilio, L. (2024). Large-scale extensional strain in Southern Tibet from Sentinel-1 InSAR and GNSS data. *Geophysical Research Letters*, 51(19), e2024GL110512. https://doi.org/10.1029/2024GL110512

Chen, M., Niu, F., Tromp, J., Lenardic, A., Lee, C. T. A., Cao, W., & Ribeiro, J. (2017). Lithospheric foundering and underthrusting imaged beneath Tibet. *Nature communications, 8(1)*, 15659. https://doi.org/10.1038/ncomms15659

Chevalier, M. L., Tapponnier, P., van Der Woerd, J., Leloup, P. H., Wang, S., Pan, J., et al. (2020). Late Quaternary extension rates across the northern half of the Yadong-Gulu rift: Implication for east-west extension in southern Tibet. *Journal of Geophysical Research: Solid Earth, 125(7)*, e2019JB019106. https://doi.org/10.1029/2019JB019106

Cocco, M., Tinti, E., & Cirella, A. (2016). On the scale dependence of earthquake stress drop. *Journal of Seismology, 20*, 1151–1170. https://doi.org/10.1007/s10950-016-9594-4

Cogan, M. J., Nelson, K. D., Kidd, W. S. F., & Wu, C. (1998). Shallow structure of the Yadong-Gulu rift, southern Tibet, from refraction analysis of Project INDEPTH common midpoint data. *Tectonics, 17(1)*, 46–61. https://doi.org/10.1029/97TC03025

Collettini, C. (2011). The mechanical paradox of low-angle normal faults: Current understanding and open questions. *Tectonophysics, 510(3-4)*, 253-268. https://doi.org/10.1016/j.tecto.2011.07.01

Cooper, F. J., Hodges, K. V., Parrish, R. R., Roberts, N. M. W., & Horstwood, M. S. A. (2015). Synchronous N–S and E–W extension at the Tibet-to-Himalaya transition in NW Bhutan. *Tectonics*, *34(7)*, 1375-1395. https://doi.org/10.1002/2014TC003712

Craig, T. J., Copley, A., & Jackson, J. (2012). Thermal and tectonic consequences of India underthrusting Tibet. *Earth and Planetary Science Letters, 353*, 231–239. https://doi.org/10.1016/j.epsl.2012.07.010

Craig, T. J., Kelemen, P. B., Hacker, B. R., & Copley, A. (2020). Reconciling geophysical and petrological estimates of the thermal structure of southern Tibet. *Geochemistry, Geophysics, Geosystems, 21*, e2019GC008837. https://doi.org/10.1029/2019GC008837

Currie, B. S., Rowley, D. B., & Tabor, N. J. (2005). Middle Miocene paleoaltimetry of southern Tibet: Implications for the role of mantle thickening and delamination in the Himalayan orogen. *Geology, 33(3)*, 181–184. https://doi.org/10.1130/G21170.1

Davies, J. H., & von Blanckenburg, F. (1995). Slab breakoff: a model of lithosphere detachment and its test in the magmatism and deformation of collisional orogens. *Earth and Planetary Science Letters, 129*, 85–102. https://doi.org/10.1016/0012-821X(94)00237-S

Dong, H., Wei, W., Jin, S., Ye, G., Jones, A. G., Zhang, L., et al. (2020). Shaping the surface deformation of central and south Tibetan Plateau: Insights from magnetotelluric array data. *Journal of Geophysical Research: Solid Earth, 125*, e2019JB019206. https://doi.org/ 10.1029/2019JB019206

Ekström, G., Nettles, M., & Dziewoński, A. M. (2012). The global CMT project 2004–2010: Centroid-moment tensors for 13,017 earthquakes [Dataset]. *Physics of the Earth and Planetary Interiors*, 200, 1–9. https://doi.org/10.1016/j.pepi.2012.04.002, last accessed 21 November 2025.

Elliott, J. R., Walters, R. J., & Wright, T. J. (2016). The role of space-based observation in understanding and responding to active tectonics and earthquakes. *Nature communications*, 7(1), 13844. https://doi.org/10.1038/ncomms13844

Elliott, J. R., Walters, R. J., England, P. C., Jackson, J. A., Li, Z., & Parsons, B. (2010). Extension on the Tibetan plateau: recent normal faulting measured by InSAR and body wave seismology. *Geophysical Journal International, 183(2)*, 503–535. https://doi.org/10.1111/j.1365-246X.2010.04754.x

England, P. C., Walker, R. T., Fu, B., & Floyd, M. A. (2013). A bound on the viscosity of the Tibetan crust from the horizontality of palaeolake shorelines. *Earth and Planetary Science Letters, 375*, 44–56. https://doi.org/10.1016/j.epsl.2013.05.001

England, P., & Houseman, G. (1986). Finite strain calculations of continental deformation: 2. Comparison with the India-Asia collision zone. *Journal of Geophysical Research: Solid Earth, 91(B3)*, 3664–3676. https://doi.org/10.1029/JB091iB03p03664

England, P., & Houseman, G. (1989). Extension during continental convergence, with application to the Tibetan Plateau. *Journal of Geophysical Research: Solid Earth, 94(B12)*, 17561–17579. https://doi.org/10.1029/JB094iB12p17561

England, P., & Molnar, P. (1997). Active deformation of Asia: From kinematics to dynamics. *Science, 278(5338)*, 647-650. https://doi/org/10.1126/science.278.5338.647

Fang, J., Houseman, G. A., Wright, T. J., Evans, L. A., Craig, T. J., Elliott, J. R., & Hooper, A. (2024). The dynamics of the India–Eurasia collision: Faulted viscous continuum models constrained by high- resolution Sentinel-1 InSAR and GNSS velocities. *Journal of Geophysical Research: Solid Earth, 129*, e2023JB028571. https://doi.org/10.1029/ 2023JB028571

Fang, J., Ou, Q., Wright, T. J., Okuwaki, R., Amey, R. M., Craig, T. J., et al. (2022). Earthquake cycle deformation associated with the 2021 Mw 7.4 Maduo (Eastern Tibet) earthquake: An intrablock rupture event on a slow-slipping fault from Sentinel-1 InSAR and teleseismic data. *Journal of Geophysical Research: Solid Earth, 127(11)*, e2022JB024268. https://doi.org/10.1029/2022JB024268

Farr, T. G., Rosen, P. A., Caro, E., Crippen, R., Duren, R., Hensley, S., et al. (2007). The shuttle radar topography mission. *Reviews of geophysics*, *45*(2). https://doi.org/10.1029/2005RG000183

Funning, G. J., Parsons, B., & Wright, T. J. (2007). Fault slip in the 1997 Manyi, Tibet earthquake from linear elastic modelling of InSAR displacements. *Geophysical Journal International, 169(3),* 988–1008. https://doi.org/10.1111/j.1365-246X.2006.03318.x

Galetzka, J., Melgar, D., Genrich, J. F., Geng, J., Owen, S., Lindsey, E. O., et al. (2015). Slip pulse and resonance of the Kathmandu basin during the 2015 Gorkha earthquake, Nepal. *Science*, 349(6252), 1091–1095. https://doi.org/10.1126/science.aac63

Garzione, C. N., DeCelles, P. G., Hodkinson, D. G., Ojha, T. P., & Upreti, B. N. (2003). East–west extension and Miocene environmental change in the southern Tibetan plateau: Thakkhola graben, central Nepal. *Geological Society of America Bulletin, 115(1)*, 3–20. https://doi.org/10.1130/0016-7606(2003)115<0003:EWEAME>2.0.CO;2

Ge, W. P., Molnar, P., Shen, Z. K., & Li, Q. (2015). Present-day crustal thinning in the southern and northern Tibetan Plateau revealed by GPS measurements. *Geophysical Research Letters, 42(13)*, 5227–5235. https://doi.org/10.1002/2015GL064347

Ha, G., Wu, Z., & Liu, F. (2019). Late quaternary vertical slip rates along the southern Yadong–Gulu Rift, southern Tibetan plateau. *Tectonophysics, 755*, 75-90. https://doi.org/10.1016/j.tecto.2019.02.014

He, P., Hetland, E. A., Niemi, N. A., Wang, Q., Wen, Y., & Ding, K. (2018). The 2016 Mw 6.5 Nura earthquake in the Trans Alai range, northern Pamir: possible rupture on a back-thrust fault constrained by Sentinel-1A radar interferometry. *Tectonophysics*, 749, 62-71. https://doi.org/10.1016/j.tecto.2018.10.025

He, P., Wen, Y., Ding, K., & Xu, C. (2020). Normal faulting in the 2020 Mw 6.2 Yutian event: implications for ongoing E–W thinning in northern Tibet. *Remote Sensing, 12(18)*, 3012. https://doi.org/10.3390/rs12183012

Hecker, S., Dawson, T. E., & Schwartz, D. P. (2010). Normal-faulting slip maxima and stress-drop variability: A geological perspective. *Bulletin of the Seismological Society of America, 100(6)*, 3130-3147. https://doi.org/10.1785/0120090356

Heimann, S., Vasyura-Bathke, H., Sudhaus, H., Isken, M. P., Kriegerowski, M., Steinberg, A., & Dahm, T. (2019). A Python framework for efficient use of pre-computed Green's functions in seismological and other physical forward and inverse source problems. *Solid Earth, 10(6),* 1921–1935. https://doi.org/10.5194/se-10-1921-2019

Hong, S., Liu, M., Zhou, X., Meng, G., & Dong, Y. (2023). Afterslip on conjugate faults of the 2020 Mw 6.3 Nima earthquake in the central Tibetan Plateau: Evidence from InSAR measurements. *Bulletin of the Seismological Society of America*, 113, 2026–2040. https://doi.org/10.1785/0120220247

Houseman, G. A., & Molnar, P. (1997). Gravitational (Rayleigh–Taylor) instability of a layer with non-linear viscosity and convective thinning of continental lithosphere. *Geophysical Journal International, 128(1)*, 125–150. https://doi.org/10.1111/j.1365-246X.1997.tb04075.x

Huangfu, P., Li, Z. H., Fan, W., Zhang, K. J., & Shi, Y. (2022). Contrasting collision-induced far-field orogenesis controlled by thermo-rheological properties of the composite terrane. *Gondwana Research, 103*, 404–423. https://doi.org/10.1016/j.gr.2021.10.020

Jackson, J. A., & White, N. J. (1989). Normal faulting in the upper continental crust: observations from regions of active extension. *Journal of Structural Geology, 11(1-2)*, 15–36. https://doi.org/10.1016/0191-8141(89)90033-3

Jay, C. N., Flesch, L. M., & Bendick, R. O. (2018). Kinematics and dynamics of the Pamir, central Asia: Quantifying the roles of continental subduction in force balance. *Journal of Geophysical Research: Solid Earth, 123(9)*, 8161–8179. https://doi.org/10.1029/2018JB015615

Jiang, S., Jiang, Y., Liu, Y., Li, S., Zhang, W., Wang, G., et al. (2021). The Bangong–Nujiang suture zone, Tibet Plateau: its role in the tectonic evolution of the eastern Tethys Ocean. *Earth-Science Reviews, 218*, 103656. https://doi.org/10.1016/j.earscirev.2021.103656

Kapp, P., Taylor, M., Stockli, D., & Ding, L. (2008). Development of active low-angle normal fault systems during orogenic collapse: Insight from Tibet. *Geology, 36(1)*, 7–10. https://doi.org/10.1130/G24054A.1

Kapp, P., Yin, A., Harrison, T. M., & Ding, L. (2005). Cretaceous-Tertiary shortening, basin development, and volcanism in central Tibet. *Geological Society of America Bulletin, 117(7-8)*, 865–878. https://doi.org/10.1130/B25595.1

Kostrov, V. V. (1974). Seismic moment and energy of earthquakes and seismic flow of rock. *Izvestiya, Academic Science USSR Physical. Earth Physics*, 1, 23–40.

Laske, G., Masters., G., Ma, Z., & Pasyanos, M. (2013). Update on CRUST1.0–A 1-degree global model of earth's crust, *Geophysics Research Abstracts, 15*, Abstract EGU2013-2658.

Lasserre, C., Peltzer, G., Crampé, F., Klinger, Y., van Der Woerd, J., & Tapponnier, P. (2005). Coseismic deformation of the 2001 Mw 7.8 Kokoxili earthquake in Tibet, measured by synthetic aperture radar interferometry. *Journal of Geophysical Research: Solid Earth*, 110(B12). https://doi.org/10.1029/2004JB003500

Leonard, M. (2010). Earthquake fault scaling: Self-consistent relating of rupture length, width, average displacement, and moment release. *Bulletin of the Seismological Society of America, 100(5A)*, 1971–1988. https://doi.org/10.1785/0120090189

Li, J., & Song, X. (2018). Tearing of Indian mantle lithosphere from high-resolution seismic images and its implications for lithosphere coupling in southern Tibet. *Proceedings of the National Academy of Sciences, 115(33)*, 8296–8300. https://doi.org/10.1073/pnas.17172581

Li, Y., Liu, X., Rodkin, M., & Pang, Y. (2022). Numerical simulation of fault deformation and seismic activity in the southern Qinghai–Tibet Plateau. *Journal of Seismology, 26(6)*, 1295–1308. https://doi.org/10.1007/s10950-022-10116-6

Li, Y., Wang, C., Dai, J., Xu, G., Hou, Y., & Li, X. (2015). Propagation of the deformation and growth of the Tibetan–Himalayan orogen: A review. *Earth-Science Reviews, 143*, 36–61. https://doi.org/10.1016/j.earscirev.2015.01.001

Liang, S., Gan, W., Shen, C., Xiao, G., Liu, J., Chen, W., et al. (2013). Three-dimensional velocity field of present-day crustal motion of the Tibetan Plateau derived from GPS measurements. *Journal of Geophysical Research: Solid Earth, 118(10),* 5722–5732. https://doi.org/10.1002/2013JB010503

Liang, X., Chen, Y., Tian, X., Chen, Y. J., Ni, J., Gallegos, A., et al. (2016). 3D imaging of subducting and fragmenting Indian continental lithosphere beneath southern and central Tibet using body-wave finite-frequency tomography. *Earth and Planetary Science Letters, 443*, 162–175. https://doi.org/10.1016/j.epsl.2016.03.029

Liu, M., & Yang, Y. (2003). Extensional collapse of the Tibetan Plateau: Results of three-dimensional finite element modeling. *Journal of Geophysical Research: Solid Earth, 108(B8)*. https://doi.org/10.1029/2002JB002248

Lu, H., Tian, X., Yun, K., & Li, H. (2018). Convective removal of the Tibetan Plateau mantle lithosphere by ~26 Ma. *Tectonophysics, 731*, 17–34. https://doi.org/10.1016/j.tecto.2018.03.006

Luo, H., Wang, T., & Wei, S. (2022). Systematic comparison of InSAR and seismic source models for moderate-size earthquakes in western China: Implication to the seismogenic capacity of the shallow crust. *Journal of Geophysical Research: Solid Earth, 127(10)*, e2022JB024794. https://doi.org/10.1029/2022JB024794

Masek, J. G., Isacks, B. L., Fielding, E. J., & Browaeys, J. (1994). Rift flank uplift in Tibet: Evidence for a viscous lower crust. *Tectonics, 13(3)*, 659–667. https://doi.org/10.1029/94TC00452

Massonnet, D., Rossi, M., Carmona, C., Adragna, F., Peltzer, G., Feigl, K., & Rabaute, T. (1993). The displacement field of the Landers earthquake mapped by radar interferometry. *Nature, 364(6433),* 138–142. https://doi.org/10.1038/364138a0

McMillan, M., & Schoenbohm, L. M. (2023). Diverse styles of lithospheric dripping: Synthesizing gravitational instability models, continental tectonics, and geologic observations. *Geochemistry, Geophysics, Geosystems, 24*, e2022GC010488. https://doi. org/10.1029/2022GC010488

Molnar, P., & Tapponnier, P. (1975). Cenozoic tectonics of Asia: Effects of a continental collision: Features of recent continental tectonics in Asia can be interpreted as results of the India-Eurasia collision. *Science, 189(4201)*, 419–426. https://doi.org/10.1126/science.189.4201.419

Molnar, P., & Tapponnier, P. (1978). Active tectonics of Tibet. *Journal of Geophysical Research: Solid Earth, 83(B11)*, 5361–5375. https://doi.org/10.1029/JB083iB11p05361

Molnar, P., England, P., & Martinod, J. (1993). Mantle dynamics, uplift of the Tibetan Plateau, and the Indian monsoon. *Reviews of Geophysics, 31(4)*, 357–396. https://doi.org/10.1029/93RG02030

Molnar, P., Houseman, G. A., & Conrad, C. P. (1998). Rayleigh—Taylor instability and convective thinning of mechanically thickened lithosphere: effects of non-linear viscosity decreasing exponentially with depth and of horizontal shortening of the layer. *Geophysical Journal International, 133(3)*, 568–584. https://doi.org/10.1046/j.1365-246X.1998.00510.x

Okada, Y. (1985). Surface deformation due to shear and tensile faults in a half-space. *Bulletin of the seismological society of America, 75(4)*, 1135–1154. https://doi.org/10.1785/BSSA0750041135

Pang, Y., Zhang, H., Shi, Y., & Gerya, T. (2022). Plume-Induced rifting of thickened crust: 2D numerical model and implications for N–S Rifts in Southern Tibet. *Geophysical Research Letters, 49(23)*, e2022GL101479. https://doi.org/10.1029/2022GL101479

Peltzer, G., & Tapponnier, P. (1988). Formation and evolution of strike-slip faults, rifts, and basins during the India-Asia collision: An experimental approach. *Journal of Geophysical Research: Solid Earth, 93(B12)*, 15085–15117. https://doi.org/10.1029/JB093iB12p15085

Ratschbacher, L., Krumrei, I., Blumenwitz, M., Staiger, M., Gloaguen, R., Miller, B. V., et al. (2011). Rifting and strike-slip shear in central Tibet and the geometry, age and kinematics of upper crustal extension in Tibet. *Geological Society, London, Special Publications, 353(1)*, 127–163. https://doi.org/10.1144/SP353.

Royden, L. H., Burchfiel, B. C., King, R. W., Wang, E., Chen, Z., Shen, F., & Liu, Y. (1997). Surface deformation and lower crustal flow in eastern Tibet. *Science, 276(5313)*, 788–790. https://doi.org/10.1126/science.276.5313.78

Ryder, I., Bürgmann, R., & Sun, J. (2010). Tandem afterslip on connected fault planes following the 2008 Nima–Gaize (Tibet) earthquake. *Journal of Geophysical Research: Solid Earth*, 115(B3). https://doi.org/10.1029/2009JB006423

Savage, J. C., & Simpson, R. W. (1997). Surface strain accumulation and the seismic moment tensor. *Bulletin of the Seismological Society of America*, 87(5), 1345–1353.

Schellart, W. P., Chen, Z., Strak, V., Duarte, J. C., & Rosas, F. M. (2019). Pacific subduction control on Asian continental deformation including Tibetan extension and eastward extrusion tectonics. *Nature Communications*, 10(1), 4480. https://doi.org/10.1038/s41467-019-12337-9

Schirripa Spagnolo, G., Mercuri, M., Billi, A., Carminati, E., & Galli, P. (2021). The segmented Campo Felice normal faults: Seismic potential appraisal by application of empirical relationships between rupture length and earthquake magnitude in the central Apennines, Italy. *Tectonics, 40*, e2020TC006465. https:// doi.org/10.1029/2020TC006465

Scholz, C.H. & Cowie, P.A. (1990). Determination of total strain from faulting using slip measurements, *Nature, 346*, 837–839. https://doi.org/10.1038/346837a0

Searle, M. P., Elliott, J. R., Phillips, R. J., & Chung, S. L. (2011). Crustal–lithospheric structure and continental extrusion of Tibet. *Journal of the Geological Society, 168(3)*, 633–672. https://doi.org/10.1144/0016-76492010-13

Shen, Z. K., Sun, J., Zhang, P., Wan, Y., Wang, M., Bürgmann, R., et al. (2009). Slip maxima at fault junctions and rupturing of barriers during the 2008 Wenchuan earthquake. *Nature Geoscience, 2*, 718–724. https://doi.org/10.1038/ngeo63

Shi, Z., Gao, R., Lu, Z., Li, W., Li, H., Huang, X., & Liang, H. (2022). Bidirectional subduction of the Bangong-Nujiang ocean revealed by deep-crustal seismic reflection profile. *Tectonophysics, 837*, 229455. https://doi.org/10.1016/j.tecto.2022.229455

Shin, Y. H., Shum, C. K., Braitenberg, C., Lee, S. M., Lim, M., Na, S. H., et al. (2022). Decoupled lithospheric folding, lower crustal flow channels, and the growth of Tibetan Plateau. *Geophysical Research Letters, 49(13)*, e2022GL099183. https://doi.org/10.1029/2022GL099183

Sloan, R. A., Jackson, J. A., McKenzie, D., & Priestley, K. (2011). Earthquake depth distributions in central Asia, and their relations with lithosphere thickness, shortening and extension. *Geophysical Journal International, 185(1)*, 1–29. https://doi.org/10.1111/j.1365-246X.2010.04882.x

Styron, R. H., & Hetland, E. A. (2014). Estimated likelihood of observing a large earthquake on a continental low-angle normal fault and implications for low-angle normal fault activity. *Geophysical Research Letters*, *41*(7), 2342–2350. https://doi.org/10.1002/2014GL059335

Styron, R. H., Taylor, M. H., & Murphy, M. A. (2011). Oblique convergence, arc-parallel extension, and the role of strike-slip faulting in the High Himalaya. *Geosphere, 7(2)*, 582–596. https://doi.org/10.1130/GES00606.1

Styron, R. H., Taylor, M. H., Sundell, K. E., Stockli, D. F., Oalmann, J. A., Moeller, A., et al. (2013). Miocene initiation and acceleration of extension in the South Lunggar rift, western Tibet: Evolution of an active detachment system from structural mapping and (U-Th)/He thermochronology. *Tectonics, 32(4)*, 880–907. https://doi.org/10.1002/tect.20053

Styron, R., Taylor, M., & Sundell, K. (2015). Accelerated extension of Tibet linked to the northward underthrusting of Indian crust. *Nature Geoscience, 8(2)*, 131–134. https://doi.org/10.1038/ngeo2336

Sundell, K. E., Taylor, M. H., Styron, R. H., Stockli, D. F., Kapp, P., Hager, C., et al. (2013). Evidence for constriction and Pliocene acceleration of east–west extension in the North Lunggar rift region of west central Tibet. *Tectonics, 32(5)*, 1454–1479. https://doi.org/10.1002/tect.20086

Tapponnier, P., & Molnar, P. (1976). Slip-line field theory and large-scale continental tectonics. *Nature, 264(5584)*, 319–324. https://doi.org/10.1038/264319a0

Tapponnier, P., Xu, Z., Francoise, R., Bertrand, M., Nicolas, A., Gérard, W., & Jingsui, Y. (2001). Oblique stepwise rise and growth of the Tibet Plateau. *Science, 294(5547)*, 1671–1677. https://doi.org/10.1126/science.105978

Taylor, M., & Yin, A. (2009). Active structures of the Himalayan-Tibetan orogen and their relationships to earthquake distribution, contemporary strain field, and Cenozoic volcanism. *Geosphere, 5(3)*, 199–214. https://doi.org/10.1130/GES00217.1

Taylor, M., Forte, A., Laskowski, A., & Ding, L. (2021). Active uplift of southern Tibet revealed. *GSA Today, 31(8)*, 4–10. https://doi.org/10.1130/GSATG487A.1

Taylor, M., Yin, A., Ryerson, F. J., Kapp, P., & Ding, L. (2003). Conjugate strike-slip faulting along the Bangong-Nujiang suture zone accommodates coeval east-west extension and north-south shortening in the interior of the Tibetan Plateau. *Tectonics, 22(4)*. https://doi.org/10.1029/2002TC001361

Thiede, R. C., Ehlers, T. A., Bookhagen, B., & Strecker, M. R. (2009). Erosional variability along the northwest Himalaya. *Journal of Geophysical Research: Earth Surface, 114(F1)*. https://doi.org/10.1029/2008JF001010

Tian, X., Chen, Y., Tseng, T. L., Klemperer, S. L., Thybo, H., Liu, Z., et al. (2015). Weakly coupled lithospheric extension in southern Tibet. *Earth and Planetary Science Letters, 430,* 171–177. https://doi.org/10.1016/j.epsl.2015.08.025

USGS. (2025) [Dataset]. https://earthquake.usgs.gov/earthquakes/search/, last accessed 21 November 2025.

Wang, H., Elliott, J. R., Craig, T. J., Wright, T. J., Liu-Zeng, J., & Hooper, A. (2014). Normal faulting sequence in the Pumqu–Xainza Rift constrained by InSAR and teleseismic body-wave seismology. *Geochemistry, Geophysics, Geosystems, 15(7)*, 2947–2963. https://doi.org/10.1002/2014GC005369

Wang, L., Wang, R., Roth, F., Enescu, B., Hainzl, S., & Ergintav, S. (2009). Afterslip and viscoelastic relaxation following the 1999 M 7.4 Izmit earthquake from GPS measurements [Software]. *Geophysical Journal International, 178(3)*, 1220–1237. https://doi.org/10.1111/j.1365-246X.2009.04228.x

Wang, M., & Shen, Z. K. (2020). Present-day crustal deformation of continental China derived from GPS and its tectonic implications. *Journal of Geophysical Research: Solid Earth*, 125(2), e2019JB018774. https://doi.org/10.1029/2019JB018774

Wang, Q., Zhang, P. Z., Freymueller, J. T., Bilham, R., Larson, K. M., Lai, X. A., et al. (2001). Present-day crustal deformation in China constrained by global positioning system measurements. *Science, 294(5542)*, 574–577. https:/doi.org/10.1126/science.106364

Wegnüller, U., Werner, C., Strozzi, T., Wiesmann, A., Frey, O., & Santoro, M. (2016). Sentinel-1 support in the GAMMA software. *Procedia Computer Science, 100*, 1305–1312. https://doi.org/10.1016/j.procs.2016.09.246

Wells, D. L., & Coppersmith, K. J. (1994). New empirical relationships among magnitude, rupture length, rupture width, rupture area, and surface displacement. *Bulletin of the seismological Society of America, 84(4)*, 974–1002. https://doi.org/10.1785/BSSA0840040974

Wen, Y., Li, Z., Xu, C., Ryder, I., & Bürgmann, R. (2012). Postseismic motion after the 2001 Mw 7.8 Kokoxili earthquake in Tibet observed by InSAR time series. *Journal of Geophysical Research: Solid Earth, 117(B8)*. https://doi.org/10.1029/2011JB009043

Wernicke, B. (1995). Low-angle normal faults and seismicity: A review. *Journal of Geophysical Research: Solid Earth, 100(B10)*, 20159–20174. https://doi.org/10.1029/95JB01911

Weston, J., Ferreira, A. M. G., & Funning, G. J. (2011). Global compilation of interferometric synthetic aperture radar earthquake source models: 1. Comparisons with seismic catalogs. *Journal of Geophysical Research: Solid Earth, 116(B8)*. https://doi.org/10.1029/2010JB008131

Williams, H., Turner, S., Kelley, S., & Harris, N. (2001). Age and composition of dikes in Southern Tibet: New constraints on the timing of east-west extension and its relationship to postcollisional volcanism. *Geology*, *29*(4), 339–342. https://doi.org/10.1130/0091-7613(2001)029<0339:AACODI>2.0.CO;2

Wimpenny, S., & Watson, C. S. (2021). gWFM: A global catalog of moderate-magnitude earthquakes studied using teleseismic body waves [Dataset]. *Seismological Research Letters, 92(1)*, 212–226. https://doi.org/10.1785/0220200218

Wolff, R., Hetzel, R., Dunkl, I., Xu, Q., Bröcker, M., & Anczkiewicz, A. A. (2019). High-angle normal faulting at the Tangra Yumco graben (southern Tibet) since ~15 Ma. *The Journal of Geology, 127(1)*, 15–36. https://doi.org/10.1086/700406

Wolff, R., Hetzel, R., Hölzer, K., Dunkl, I., Xu, Q., Anczkiewicz, A. A., & Li, Z. (2023). Rift propagation in south Tibet controlled by under-thrusting of India: a case study of the Tangra Yumco graben (south Tibet). *Journal of the Geological Society, 180(2)*, jgs2022-090. https://doi.org/10.1144/jgs2022-090

Wright, T. J., Houseman, G. A., Fang, J., Maghsoudi, Y., Hooper, A. J., Elliott, J. R., et al. (2026). High-resolution geodetic velocities reveal role of weak faults in deformation of Tibetan Plateau. *Science, 391(6784)*, 499–503. https://doi.org/10.1126/science.adi3552

Wrobel, A. J., Gans, P. B., & Womer, J. B. (2021). Late cretaceous crustal shortening in the northern snake range metamorphic core complex: Constraints on the structural geometry and magnitude of pre-extensional footwall burial. *Tectonics, 40(8)*, e2020TC006460. https://doi.org/10.1029/2020TC006460

Xiao, X., Cheng, S., Wu, J., Wang, W., Sun, L., Wang, X., et al. (2024). CSRM-1.0: A China seismological reference model. *Journal of Geophysical Research: Solid Earth, 129(9)*, e2024JB029520. https://doi.org/10.1029/2024JB029520

Yang, L., Liu, H., & Zhao, J. (2009). Characteristic of crustal structure beneath the rifts in southern Tibetan plateau. *Earthquake Science, 22*, 373–377. https://doi.org/10.1007/s11589-009-0373-y

Yin, A. (2000). Mode of Cenozoic east-west extension in Tibet suggesting a common origin of rifts in Asia during the Indo-Asian collision. *Journal of Geophysical Research: Solid Earth, 105(B9)*, 21745–21759. https://doi.org/10.1029/2000JB900168

Yin, A., & Harrison, T. M. (2000), Geologic evolution of the Himalayan–Tibetan orogen. *Annual review of earth and planetary sciences, 28(1)*, 211–280. https://doi.org/10.1146/annurev.earth.28.1.211

Yin, A., & Taylor, M. H. (2011). Mechanics of V-shaped conjugate strike-slip faults and the corresponding continuum mode of continental deformation. *GSA Bulletin, 123(9–10)*, 1798–1821. https://doi.org/10.1130/B30159.1

Zhang, B., Bao, X., Wu, Y., Xu, Y., & Yang, W. (2023). Southern Tibetan rifting since late Miocene enabled by basal shear of the underthrusting Indian lithosphere. *Nature Communications, 14(1)*, 2565. https://doi.org/10.1038/s41467-023-38296-w

Zhang, P. Z., Shen, Z., Wang, M., Gan, W., Burgmann, R., Molnar, P., et al. (2004). Continuous deformation of the Tibetan Plateau from global positioning system data. *Geology, 32(9)*, 809–812. https://doi.org/10.1130/G20554.1

Zheng, G., Wang, H., Wright, T. J., Lou, Y., Zhang, R., Zhang, W., et al. (2017). Crustal deformation in the India-Eurasia collision zone from 25 years of GPS measurements. *Journal of Geophysical Research: Solid Earth, 122(11)*, 9290–9312. https://doi.org/10.1002/2017JB014465

Figure Captions

Figure 1. A simplified tectonic setting of the Tibetan Plateau and its adjacent region. The focal mechanisms depict events (M ≥ 5.0) derived from the Harvard CMT catalog since 1992, and normal-faulting events marked with green color (note that these are normal-faulting events with large rake angles defined between -150 and -30°). Dark red dashed lines indicate the suture zones in the plateau. The grey belts show the rifts and grabens (Ge et al., 2015). Thick black lines show the major thrust and strike-slip boundary faults, and blue lines indicate the normal faults (Tapponnier et al., 2001). The blue rectangular frames labeled A–F denote the different local tectonic settings referenced in the following subfigures, which include normal-faulting events identified from InSAR observations in this study. For example, rectangle A shows the spatial extent of Figure 2a, while rectangles B–F indicate the spatial extents of Figures S2a–S6a in the supplementary file.

Figure 2. Local tectonic setting of the Yadong–Gulu and Amdo rifts, including interferograms of normal-faulting events from the past three decades. The colored circles, labeled with years, represent earthquakes of magnitude M ≥ 6 that have occurred on the Tibetan Plateau since 1900, as reported by the National Earthquake Data Center (NEDC) (2022). The black focal mechanisms illustrate the focal mechanisms of events (Mw ≥ 4.5) reported in the Global Centroid Moment Tensor (gCMT) catalog since 1976, while the five blue focal mechanisms indicate normal-faulting events detected by InSAR. The corresponding interferograms for these five events are shown in panels b–i. In these panels, the blue line represents the fault line projected onto the surface along its dip plane, extending upward. The black rectangular frame indicates the slip plane in the subsurface determined from the uniform slip model in this study.

Figure 3. Coseismic slip distributions for the five events in the Yadong–Gulu and Amdo region, as depicted in Figure 2. Arrows indicate the direction of motion of the hanging wall, while the contours represent the coseismic slip in meters. a, the 30 July 1992 Mw 6.0 Nyemo event. b, the 29 June 1994 Mw 6.0 Baqen event. c, the 6 October 2008 Mw 6.3 Damxung event. d, the 17 October 2016 Mw 5.9 Zaduo event. e, the 19 March 2021 Mw 5.7 Biru event.

Figure 4. Results of seismological analysis. For each earthquake, we show the probabilistic moment tensor, the probability density function for centroid depth, and two example waveforms for each of the vertical and transverse components, from different azimuths. In the waveform panels, the data are shown in black, and the best-fit synthetic data are shown in red. The inset text indicates the station ID, epicentral distance, and azimuth (above), along with the onset time and inversion window duration (below). Here we show results for earthquakes on 1994/06/29, 2003/07/07, 2004/03/27, and 2008/06/25. Equivalent figures for the other 7 earthquakes studied here are shown in the Supplementary Figures S90 and S91.

Figure 5. Normal-faulting events in the Tibetan Plateau from the ICMT and gWFM catalogs. (a) The ICMT catalog, developed as part of this study, includes events since 1992. The accompanying histograms illustrate the magnitude distributions of these events. In the inset rectangular figure, light red triangles denote the magnitude and depth of each event, with error bars indicating depth uncertainties. (b) The gWFM catalog since 1976. The blue focal mechanisms represent results from the published gWFM catalog (Wimpenny & Watson, 2021), while the green focal mechanisms indicate additional results contributed from this study. The accompanying histograms show the magnitude distributions for these events. In the inset rectangular figure, the light red squares indicate the magnitude and depth of each event, and the error bars indicate the depth uncertainties. (c) Comparison of weighted centroid depths for normal-faulting events between the ICMT and gWFM catalogs since 1992. The blue and green squares correspond to the events shown in subfigure (b), whereas the red triangles represent the events from subfigure (a), with the error bars indicating their respective depth uncertainties.

Figure 6. The scaling properties of normal-faulting events evaluated from the ICMT catalog refer to the analysis of key seismic parameters, including rupture dimensions (a), stress drop (b), and the relationship between rupture length and earthquake magnitude (c). The error bars indicate the respective rupture dimension uncertainties.

Figure 7. Recent normal-faulting events, extensional structures and initiation ages, and possible extensional patterns discussed for the Tibetan Plateau. (a) Rifts initiation age and gravity collapse extension pattern. The colored triangle pairs in the top-left corner denote locations of different extensional structures, involving N–S extension on the South Tibetan fault system (STFS), E–W extension associated with the normal faults and N–S-striking dikes. These structures are labeled in the top-right corner with names such as Fa, Zanskar, Fb. Sutlej, and so forth (Cooper et al., 2015; Li et al., 2015). For each extensional structure, initiation ages are indicated in black text with a white background and were determined via geochemical dating methods (Sundell et al., 2013; Bian et al., 2022). The legends of the numbered circles with a hot-cold color scale in the top-left corner represent recent normal-faulting events derived from the ICMT catalog in this study, and colors indicating the respective dip angle. Detailed parameters of each event can be found in Supplementary Table S5, referenced by serial numbers from 1 to 26. (b) Rifts dip angle inferred from geological survey and axial symmetry extension pattern. The legend in the bottom-right corner indicates normal faults with either high or low dip angles, as inferred from geological surveys (Wolff et al., 2019). The hot colored circle points show the distribution of dip angles for all recent normal-faulting events from the ICMT catalog in this study, similar to subfigure (a). (c) Normal-faulting events recorded in our ICMT catalog and the initiation ages of their related rifts. The numbered circles are referenced based on the serial numbers of normal-faulting events from 1 to 26, as shown in subfigure (a). (d) Relationship between the normal-faulting dip angle and tectonics on Earth. The dashed blue lines broadly categorize the dip range of normal-faulting events into low (< 35°), moderate 35°–65°, and high (> 65°) dip angles, which are typically associated with different tectonic structures

and features. The error bars in subfigure (d) indicate the respective dip angle and depth uncertainties in this study.

Figure 8. Normal-faulting events and crustal thinning. (a) Topographic areas with elevation above 5000 m and the locations of normal-faulting events. The accompanying histograms display the frequency of normal-faulting events at different elevation levels. (b) Extensional setting of dilatational strain derived from large-scale InSAR data (Wright et al., 2026), with positive dilation related to the normal-faulting events. The pink and green lines indicate the extensional regions in Yutian and the interior of the Tibetan Plateau, respectively.

Figure 9. Distribution of normal-faulting events related to crust thickness and dynamic model prediction. (a) Moho depth based on the Crust 1.0 model (Laske et al., 2013), showing that normal-faulting events generally occur within a crustal region that is at least 60 km thick. (b) Model-predicted distribution of fault types, considering the gravitational potential energy derived from the lithospheric thickness and boundary stress caused by major faults on the Tibetan Plateau (Fang et al., 2024).

Figure 1.

80˚E
84˚E
88˚E
92˚E
96˚E
40˚N
36˚N
32˚N
28˚N
Mw >= 7
6 <= Mw < 7
5 <= Mw < 6
TARIM BASIN
ALTYN TAGH FAULT
Kunlun–Qaidam Block
QAIDAM BASIN
Ayimaqin
Kunlun
Suture
Zone
Songpan–Ganze Block
KUNLUN FAULT
WEST KUNLUN SHAN
LONGMU–GOZACO
KARAKORUM FAULT
Jinsha
Jiang
Suture
Zone
Qiangtang Block
Bangong
Nujiang
Suture
Zone
Lhasa Block
Indus
Yalu
Suture
Zone
Himalaya Block
HIMALAYAN FRONTAL THRUST
55 mm/yr
INDIA
200 km
A
B
C
D
E
F
m
8500
8000
7500
7000
6500
6000
5500
5000
4500
4000
3500
3000
2500
2000
1500
1000
500
0

Figure 2.

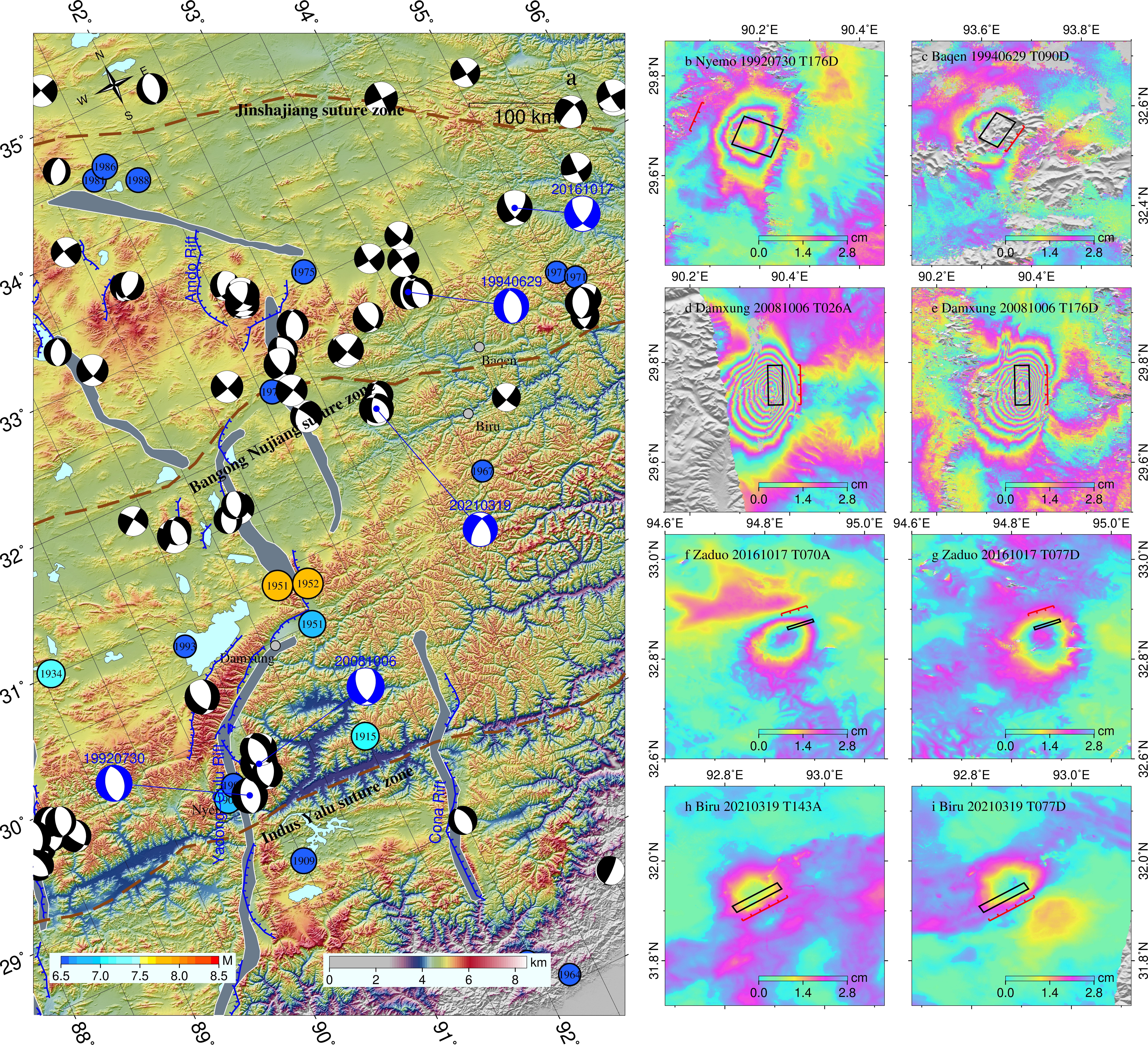

a
Jinshajiang suture zone
100 km
Bangong Nujiang suture zone
Indus Yalu suture zone
Amdo Rift
Yadong-Gulu Rift
Cona Rift
Baqen
Biru
Damxung
Nyemo
20161017
19940629
20210319
20081006
19920730
1986
1981
1988
1975
1971
1967
1951
1952
1993
1934
1915
1909
1964
M
6.5
7.0
7.5
8.0
8.5
km
0
2
4
6
8
b Nyemo 19920730 T176D
c Baqen 19940629 T090D
d Damxung 20081006 T026A
e Damxung 20081006 T176D
f Zaduo 20161017 T070A
g Zaduo 20161017 T077D
h Biru 20210319 T143A
i Biru 20210319 T077D
cm
0.0
1.4
2.8

Figure 3.

a Nyemo 19920730
b Baqen 19940629
c Damxung 20081006
d Zaduo 20161017
e Biru 20210319
Along Dip Width (km)
Depth (km)
Along Strike Length (km)
m
0.00 0.25 0.50
0.00 0.15 0.30
0.0 0.5 1.0
0.0 0.1 0.2

Figure 4.

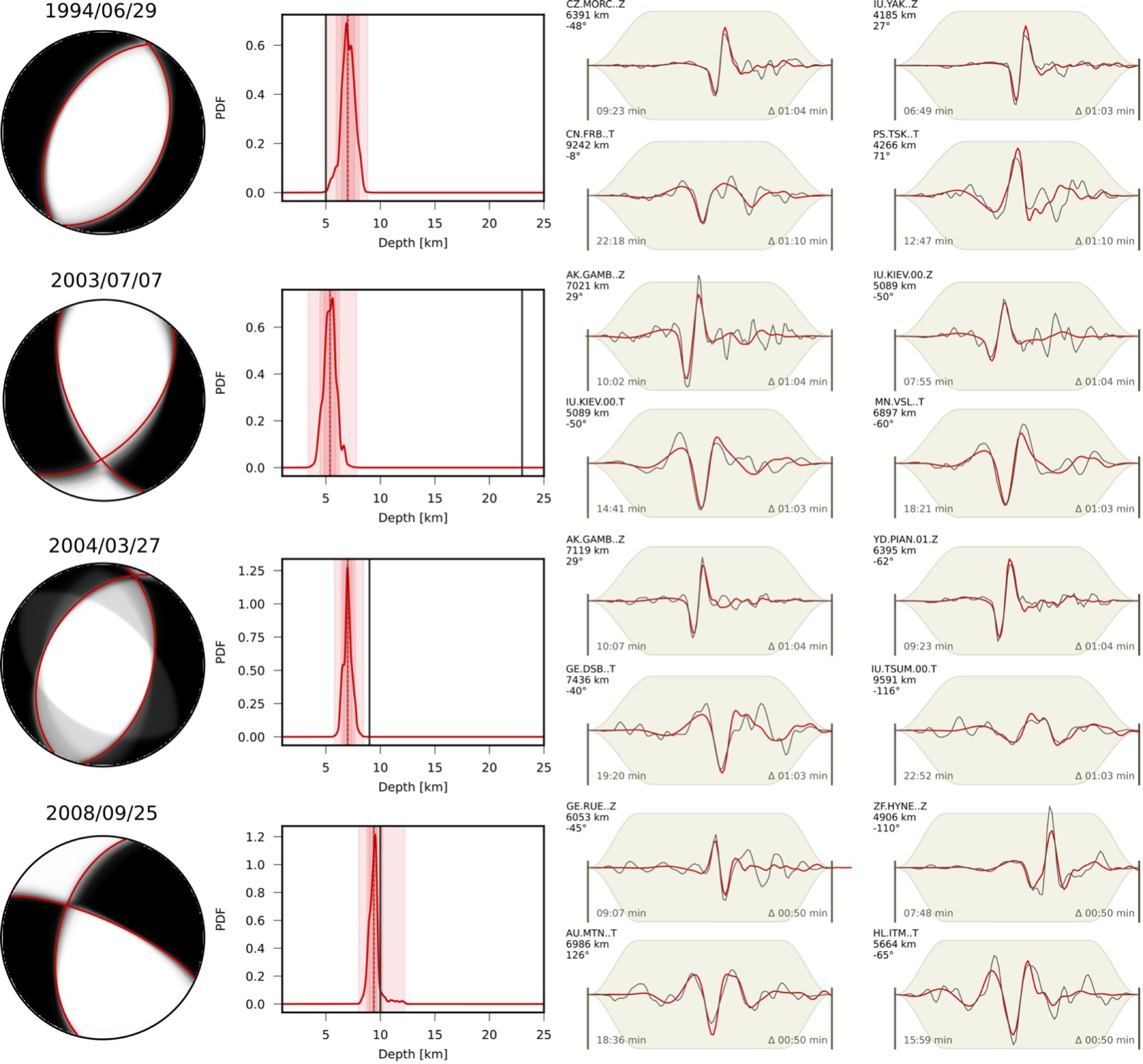
1994/06/29
2003/07/07
2004/03/27
2008/09/25
PDF
Depth [km]
CZ.MORC..Z
6391 km
-48°
09:23 min
Δ 01:04 min
IU.YAK..Z
4185 km
27°
06:49 min
Δ 01:03 min
CN.FRB..T
9242 km
-8°
22:18 min
Δ 01:10 min
PS.TSK..T
4266 km
71°
12:47 min
Δ 01:10 min
AK.GAMB..Z
7021 km
29°
10:02 min
Δ 01:04 min
IU.KIEV.00.Z
5089 km
-50°
07:55 min
Δ 01:04 min
IU.KIEV.00.T
5089 km
-50°
14:41 min
Δ 01:03 min
MN.VSL..T
6897 km
-60°
18:21 min
Δ 01:03 min
AK.GAMB..Z
7119 km
29°
10:07 min
Δ 01:04 min
YD.PIAN.01.Z
6395 km
-62°
09:23 min
Δ 01:04 min
GE.DSB..T
7436 km
-40°
19:20 min
Δ 01:03 min
IU.TSUM.00.T
9591 km
-116°
22:52 min
Δ 01:03 min
GE.RUE..Z
6053 km
-45°
09:07 min
Δ 00:50 min
ZF.HYNE..Z
4906 km
-110°
07:48 min
Δ 00:50 min
AU.MTN..T
6986 km
126°
18:36 min
Δ 00:50 min
HL.ITM..T
5664 km
-65°
15:59 min
Δ 00:50 min

Figure 5.

a ICMT catalog
b gWFM catalog
c Comparison between ICMT and gWFM
published gWFM catalog
updated in this study
gWFM
ICMT
80˚E
84˚E
88˚E
92˚E
36˚N
32˚N
28˚N
LONGMU–GUOZACO
KUNLUN FAULT
HIMALAYAN FRONTAL THRUST
Yibug Caka–RigainPun Co
Yari R.
Gurla Mandhata R.
Thakkhola R.
Xiakangjian R.
Kung Co R.
Tangra–Yum Co R.
Amdo R.
200 km
Number
Mw
Depth (km)
Time

Figure 6.

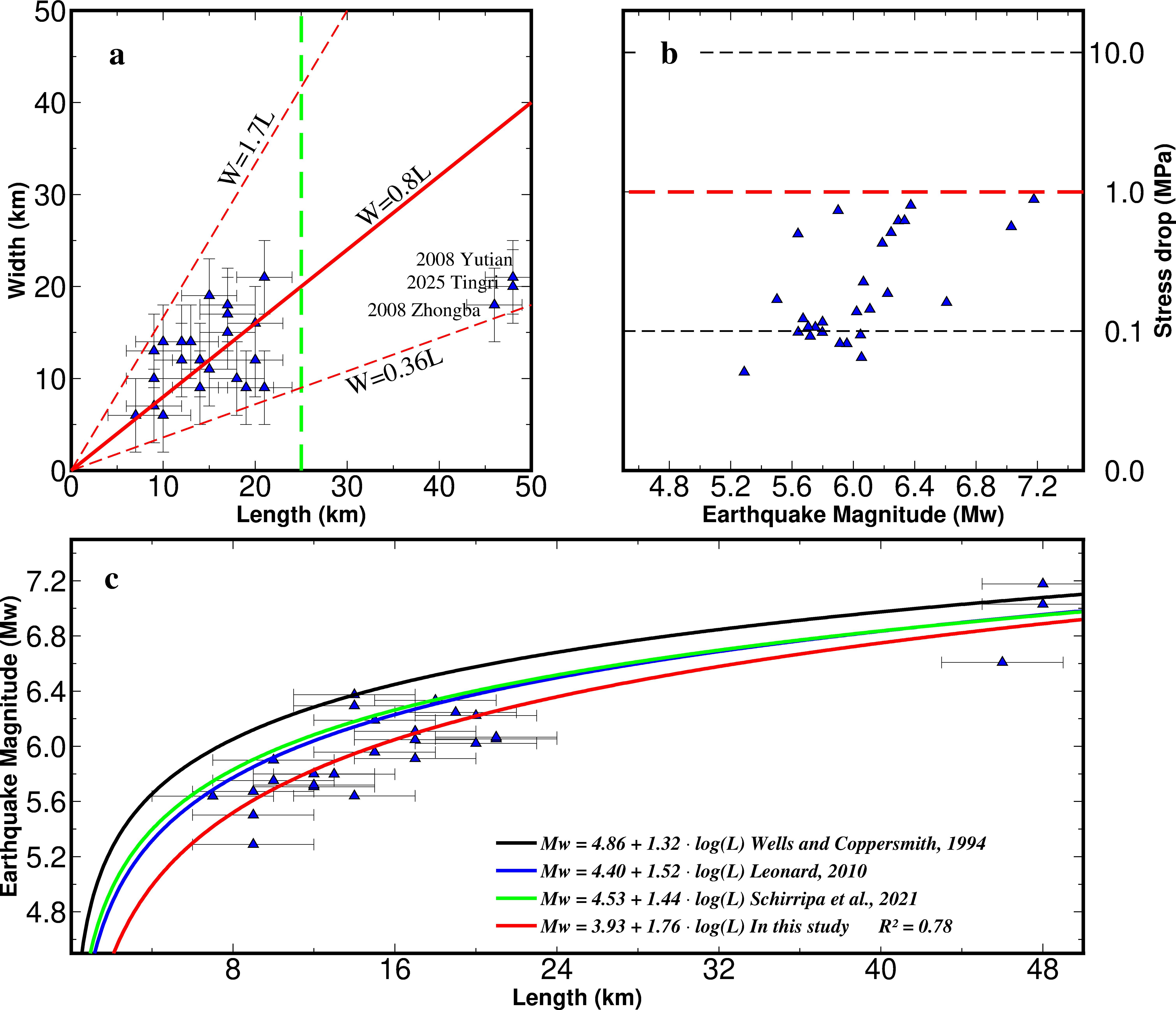
a
W=1.7L
W=0.8L
W=0.36L
2008 Yutian
2025 Tingri
2008 Zhongba
Width (km)
Length (km)
b
Stress drop (MPa)
Earthquake Magnitude (Mw)
c
Earthquake Magnitude (Mw)
Length (km)
Mw = 4.86 + 1.32 · log(L) Wells and Coppersmith, 1994
Mw = 4.40 + 1.52 · log(L) Leonard, 2010
Mw = 4.53 + 1.44 · log(L) Schirripa et al., 2021
Mw = 3.93 + 1.76 · log(L) In this study R² = 0.78

Figure 7.

a Rift initation age and gravity collapse pattern
N–S extension on STFS
N–S striking dikes
E–W normal faults
Fa. Zanskar
Fb. Sutlej
Fc. Shivling
Fd. Manaslu
Fe. Langtang
Ff. Everest
Fg. Dinggye
Fh. Sikkim
Fi. Masang Kang
Fj. Khula Kangri
Sa. Leo Pargil
Sb. Gurla Mandhata
Sc. South Lunggar
Sd. North Lunggar
Se. Thakkhola
Sf. Lopukangri
Sg. Kung Co
Sh. Tangra Yumco
Si. Ama Drime
Sj. Xainza
Sk. Yadong
Sl. Gyangze
Sm. Ringbung
Sn. Nyainqentanghla
So. Gulu
Sp Amdo–Cona
Sq. Cona
Sr. Shuang Hu
Ta. Daggyai
Tb. Pabbai
Tc. Xigaze
Source parameters in this study
Mw 6.5 event with number #10
Mw 5.5 event with number #12
Dip (°)
ALTYN TAGH FAULT
KUNLUN SHAN
LONGMU–GUOZACO
KARAKORUM FAULT
South Tibetan Fault System (STFS)
HIMALAYAN FRONTAL THRUST
b Geological fault dip angle and axial symmetry pattern
200 km
WEST KUNLUN SHAN
QAIDAM BASIN
KUNLUN FAULT
High–angle normal faults
1 Tangra Yumco
2 Lopukangri
3 Xainza
4 Thakkhola
5 Kung Co
6 Dinggye
7 Shuang Hu
Low–angle normal faults
8 Lunggar
9 Nyainqentanghla
10 Leo Pargil
11 Gurla Mandhata
12 Yadong
c Normal fault events and the rifts initation age
Dip (°)
Initation Age (Ma)
d Dip angle and depth
Depth (km)
Dip (°)
Core–complex domes, oceanic detachments, deep continent rifts.
low angle (<35°)
Common extensional structures found in the upper crust
moderate angle (35° ~ 65°)
Rapidly rising, young tectonics, and volcanic areas.
high angle (>65°)

Figure 8.

80°E
84°E
88°E
92°E
36°N
32°N
28°N
a Topography
b Dilatation
Kunlun
Suture
Ayimaqin
Zone
LONGMU-GOZHA
Jinsha
Jiang
Suture
Zone
Bangong
Nujiang
Suture
Zone
Indus
Yalu
Suture
Zone
HIMALAYAN FRONTAL THRUST
Numbers
Elevation (m)
200 km
0 1000 2000 3000 4000 5000 6000 7000 8000
m
-50
0
50
10^{-9}/yr

Figure 9.


80˚E
84˚E
88˚E
92˚E
36˚N
32˚N
28˚N
a Moho depth
LONGMU–GUOZAO
HIMALAYAN FRONTAL THRUST
200 km
20
40
60
80
km
b Model–predicted distribution of fault types
RR
RS
SR
SN
NS
NN
P
0.000
0.250
0.375
0.500
0.625
0.750
1.000